Earth's Future

RESEARCH ARTICLE
10.1029/2025EF005938

Drivers of CMIP Tropical Pacific Warming Pattern Diversity

V. Danielli[1], M. Lengaigne[1], K. Sadhvi[2], S. Gopika[3,4], and J. Vialard[5]

[1]MARBEC, University of Montpellier, IFREMER, IRD, Paris Cedex 05, France, [2]Digital University Kerala (DUK), Trivandrum, India, [3]CSIR- National Institute of Oceanography, Goa, India, [4]School of Earth, Ocean and Atmospheric Sciences, Goa University, Goa, India, [5]LOCEAN/IPSL, Sorbonne Universités (UPMC, University Paris 06)-CNRS-IRD-MNHN, Paris, France

Abstract Anthropogenic changes in sea surface temperature relative to the tropical mean (relative SST) play a pivotal role in influencing atmospheric stability and circulation. In the tropical Pacific, CMIP5/6 multi-model mean (MMM) projections by the end of the 21st century show a southeastern relative cooling and a reduced equatorial SST gradient, although individual models exhibit considerable diversity. Using a simplified heat budget framework, we analyze the processes driving these relative SST changes across 63 CMIP5/6 models under historical and most pessimistic future scenarios. In the southeastern tropical Pacific, MMM relative SST cooling is driven by intensified winds that enhance latent heat flux, with inter-model diversity explained by variations in clouds and winds. Conversely, the MMM equatorial SST gradient reduction arises from reduced evaporative cooling efficiency in the climatologically cold eastern Pacific. A heat budget covariance analysis reveals that inter-model diversity in equatorial Pacific warming is predominantly driven by ocean dynamical processes, challenging previous studies that emphasized cloud feedback mechanisms. Clouds instead mitigate inter-model spread. The inter-model spread in ocean dynamics is linked to two factors: trade wind relaxation and the cold tongue bias. Stronger trade wind relaxation amplifies western Pacific warming, while a weaker cold tongue indicates a less effective ocean thermostat, enhancing eastern Pacific warming. During the present-day period, only a subset of models captures the observed equatorial SST gradient strengthening, but the mechanisms vary across these models, complicating the identification of robust drivers of this observed trend.

Plain Language Summary Climate change warms the tropical Pacific Ocean unevenly, with some regions warming more than others. These regional differences are important because they influence atmospheric stability, rainfall, winds, and tropical cyclones. In the southeastern Pacific, climate models project less warming in the future, driven by stronger winds that increase evaporation, cooling the ocean surface. Wind and cloud changes further amplify or dampen this effect depending on the model. In the equatorial Pacific, models project more warming in the east compared to the west due to reduced evaporative cooling over cold eastern Pacific waters. Variations among models in this area are linked to oceanic dynamics, rather than cloud feedback as previously thought. When examining recent present-day trends, only some models replicate the observed subdued warming in the equatorial Pacific. However, the physical mechanisms underlying these model projections differ, complicating efforts to identify the primary driver of observed trends.

Key Points:

- The southeastern Pacific relative cooling and its inter-model diversity are primarily driven by enhanced evaporation caused by strengthened trade winds
- Mean El Niño-like warming is controlled by differential evaporative cooling, inter-model diversity by ocean processes
- Diverse atmospheric and oceanic processes reproduce observed eastern Pacific cooling, complicating model-observation reconciliation

Supporting Information:

Supporting Information may be found in the online version of this article.

Correspondence to:

V. Danielli,
danielli.vincent@ird.fr

Citation:

Danielli, V., Lengaigne, M., Sadhvi, K., Gopika, S., & Vialard, J. (2025). Drivers of CMIP tropical Pacific warming pattern diversity. *Earth's Future*, *13*, e2025EF005938. https://doi.org/10.1029/2025EF005938

Received 10 JAN 2025
Accepted 25 JUN 2025

Author Contributions:

Conceptualization: V. Danielli, M. Lengaigne, K. Sadhvi, J. Vialard
Data curation: V. Danielli
Formal analysis: V. Danielli, M. Lengaigne
Investigation: V. Danielli, M. Lengaigne, J. Vialard
Methodology: V. Danielli, M. Lengaigne, K. Sadhvi, S. Gopika, J. Vialard
Resources: V. Danielli
Software: V. Danielli, K. Sadhvi, S. Gopika, J. Vialard
Supervision: M. Lengaigne
Validation: V. Danielli, M. Lengaigne, J. Vialard

1. Introduction

Since the pre-industrial era, anthropogenic greenhouse gas emissions have increased sea surface temperatures (SST; see Table 1 for all acronyms). However, this warming is uneven (IPCC Sixth Assessment Report), with regions warming more or less than the tropical mean. These deviations, captured as relative SST, alter atmospheric vertical stability and are closely linked to shift in rainfall patterns (e.g., Izumo et al., 2020; Johnson & Xie, 2010), often described as the "warmer gets wetter" effect. Such changes influence tropical winds, mid-latitude teleconnections, and tropical cyclone distribution (Sobel et al., 2023; Xie, 2020).

Most climate models participating in the Coupled Model Intercomparison Project (CMIP) project consistent tropical Pacific warming patterns (TPWP; Huang & Ying, 2015), including subdued warming in the southeastern Pacific (SEP) and enhanced equatorial warming (Figure 1a; Liu et al., 2005; Xie et al., 2010). The latter, most pronounced in the eastern equatorial Pacific (EEP), creates an "El Niño-like" warming pattern (Huang & Ying, 2015; Vecchi et al., 2008; Ying et al., 2015), intensifying equatorial rainfall and altering the frequency of

Visualization: M. Lengaigne
Writing – original draft: V. Danielli
Writing – review & editing: M. Lengaigne, J. Vialard

Table 1
List of Acronyms and Symbols Used in This Study

Usage	Acronym	Definition
General	MMM	Multi-Model Mean
	TPWP	Tropical Pacific Warming Pattern
	SST/T	Sea Surface Temperature
	T'	Relative Sea Surface Temperature
Regions	EEP	Eastern Equatorial Pacific (2°N–2°S, 140°W–90°W)
	SEP	Southeastern Pacific (12°S–22°S, 80°W–130°W)
	WEP	Western Equatorial Pacific (2°N–2°S, 150°E–160°W)
Fluxes	LH	Latent Heat Flux
	LWD	Downward Longwave radiation
	LWU	Upward Longwave radiation
	SH	Sensible Heat Flux
	SW	Shortwave radiation
	Q	Net Heat Flux
	O	Ocean processes
	α	Heat flux feedback coefficient
Notation	Δ	Future change (2075/2100 minus 1900/1925)
	Δ_{pres}	Present-day change (2000/2020 minus 1980/2000)
	$\overline{X}$	Tropical mean of a given variable X
	X'	Deviation from tropical mean of a given variable X
	<X>	Multi-Model Mean of a given variable
	X^*	Value of a variable divided by MMM α (< α >)
	X_{For}	"Forcing" component of heat flux (independent of local SST changes)

extreme rainfall during El Niño events (Cai et al., 2014). The TPWP also modulates global climate feedbacks (Stevens et al., 2016), making it a key focus in climate science (Watanabe et al., 2024).

Observations over recent decades, however, suggest a contrasting "La Niña-like" warming pattern, characterized by subdued equatorial warming, a strengthened SST gradient and stronger trade winds (Seager et al., 2019, 2022; Watanabe et al., 2021; Wills et al., 2022). This discrepancy between observed trends and present-day simulations has sparked debates about whether models misrepresent the forced response or underestimate internal variability (Lee et al., 2022; Watanabe et al., 2024).

Despite some commonalities, CMIP models display considerable diversity in their TPWP projections (Huang & Ying, 2015). Variations are particularly prominent in the western and in the EEP, as well as along the northern edge of the SEP's subdued warming (Figure 1b). The inter-model spread in the Western Equatorial Pacific (WEP) exceeds the multi-model mean (MMM), driven by a few models that simulate a "La Niña-like" pattern similar to recent observational trends (Gopika et al., 2024; Heede & Fedorov, 2023). Understanding the mechanisms behind this diversity is critical for improving the reliability of future projections (Heede et al., 2021; Heede & Fedorov, 2021).

Thermodynamical processes play a central role in shaping TPWP. The Clausius-Clapeyron relation implies a weaker evaporative cooling in the colder EEP, amplifying warming and contributing to the "El Niño-like" pattern (Fu & Fedorov, 2023; Heede et al., 2020; Xie et al., 2010; Zhang & Li, 2014). Clouds have a spatially varying relation to SST. A warming destabilizes the atmosphere leading to more clouds in the central Pacific convective region, but less clouds in the low-cloud regions of the eastern Pacific, leading to an El Niño like warming (Ramanathan & Collins, 1991). Southern Ocean cooling contributes to the tropical SEP's cooling via wind-driven advection and atmosphere–ocean feedbacks, which may have strengthened the equatorial SST gradient in recent decades (Dong et al., 2022; Kang et al., 2023; Kim et al., 2022). Additionally, changes in anthropogenic sulfate

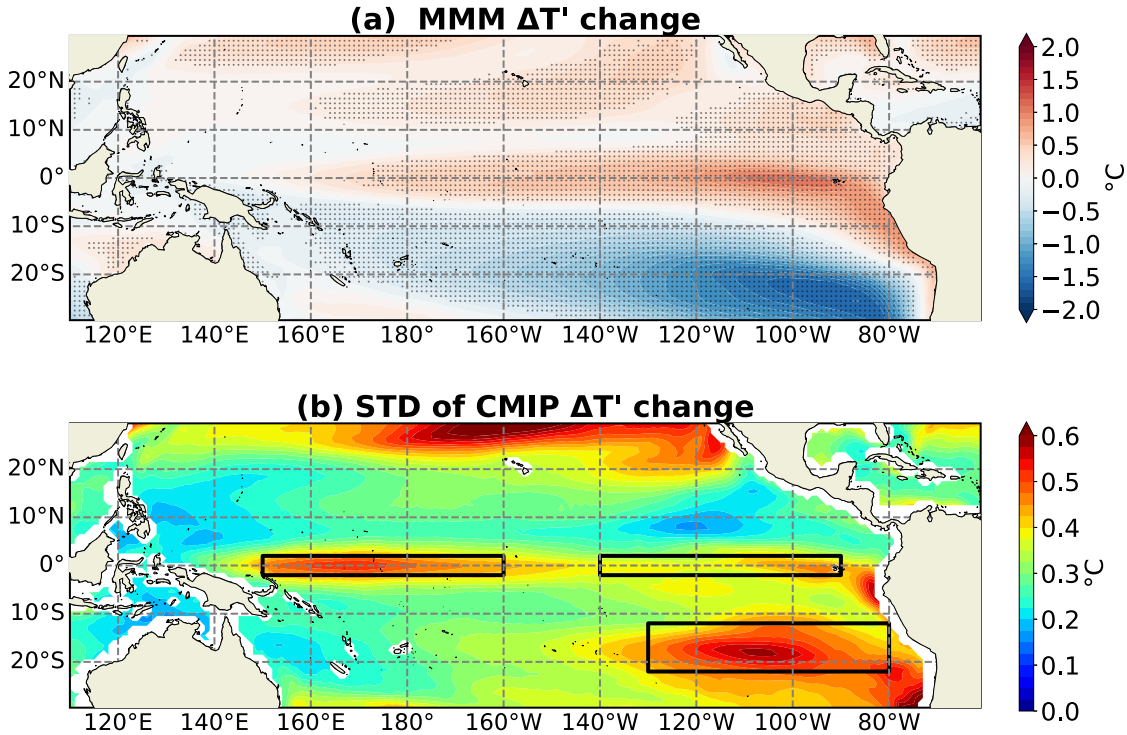

Figure 1. Multi-Model Mean (MMM) Tropical Pacific warming pattern and its inter-model diversity from Coupled Model Intercomparison Project (CMIP) simulations: (a) CMIP MMM relative SST change ($\Delta T'$). Dotted areas indicate regions where more than 75% of models agree on the sign of the MMM change. (b) Inter-model standard deviation of $\Delta T'$. Highlighted boxes denote the focus regions: western equatorial Pacific, eastern equatorial Pacific and southeastern Pacific.

aerosol emissions could have influenced the recent equatorial Pacific cooling trend (Heede & Fedorov, 2021; Hwang et al., 2024).

Oceanic and air-sea coupled processes also significantly influence changes in equatorial SST gradients. The ocean thermostat mechanism (Clement et al., 1996) can contribute to La Niña-like conditions by bringing relatively cool deep waters to the surface, less influenced by anthropogenic effects (Clement et al., 1996; DiNezio et al., 2009). However, this mechanism is transient, becoming less effective as heat penetrates deeper ocean layers over time (Heede et al., 2020). Changes in heat transport by the Pacific subtropical cells also influence zonal SST gradients. For example, advection of warm extratropical water by subtropical cells (Kang et al., 2020; Tseng et al., 2023) or a weakening of these cells (Stuecker et al., 2020) has been linked to the projected weakening of the equatorial zonal SST gradient in CMIP models. The Bjerknes feedback (Bjerknes, 1969), a key process in El Niño-Southern Oscillation variability, could also amplify equatorial relative SST changes, regardless of whether the warming pattern is El Niño-like or La Niña-like. This feedback, driven by the coupling between the zonal SST gradient, equatorial trade winds, and the thermocline slope, may account for about half of the observed changes in the SST (Fu & Fedorov, 2023). Interactions between tropical ocean basins could also contribute: enhanced Indian and Atlantic Oceans warming may strengthen equatorial Pacific trade winds and zonal SST gradient (Cai et al., 2019).

While differential evaporative damping is widely recognized as the main driver of the MMM "El Niño-like" warming (Heede et al., 2020; Xie et al., 2010; Zhang & Li, 2014), the mechanisms driving inter-model diversity remain unresolved. Some studies have linked the diversity of TPWP patterns to historical model biases (Huang & Ying, 2015; Zhou & Xie, 2015), while others alternatively attributed diversity to cloud–radiation feedback (Ying & Huang, 2016) or oceanic processes (Park et al., 2022).

This study aims to identify the mechanisms driving both the MMM TPWP and its inter-model diversity across CMIP5 and CMIP6 models. Building on the simplified ocean heat budget framework of Zhang and Li (2014; hereafter ZL14), our approach introduces several key innovations. First, we derive a new analytical formulation of the heat budget tailored specifically for relative SST changes, enabling a more direct attribution of warming

pattern drivers than the absolute temperature framework used in ZL14. Second, we apply this framework to an expanded ensemble of 63 models, significantly exceeding the sample sizes used in prior studies (e.g., 17 CMIP5 models in ZL14; 21 CMIP5 and 25 CMIP6 models in Park et al., 2022), which allows a more robust statistical characterization of inter-model spread and intergenerational comparisons between CMIP5 and CMIP6. Third, we implement a variance (covariance) decomposition of the relative SST heat budget, quantifying the relative contributions of ocean dynamics, radiative forcing, and feedback inhomogeneity to model spread. This methodological advance helps reconcile conflicting interpretations in the literature regarding the dominant sources of uncertainty, such as the contrasting emphasis on cloud feedback versus oceanic processes in Ying and Huang (2016) and Park et al. (2022). Finally, by applying this analysis to both future projections and the recent period, we bridge the gap between modeled and observed SST trends, offering insights into the origins of the apparent discrepancy between past observations and future projections of the equatorial Pacific SST gradient.

This paper is structured as follows. Section 2 provides an overview of the CMIP data set and its processing, briefly reviews the ZL14 heat budget equation, and derives a new equation for projected relative SST change. Section 3 examines the drivers of the MMM TPWP projected by the end of the 21st century, while Section 4 investigates the drivers of its inter-model diversity. Section 5 discusses the drivers of TPWP over the present-day period, focusing on the models that simulate an equatorial cooling trend, as observed. Section 6 provides a summary and discussion of our results in the context of previously published literature.

2. Material and Methods

2.1. CMIP Data and Processing

We analyze outputs from 63 CMIP models: 27 from CMIP5 (Taylor et al., 2012) and 36 from CMIP6 (Eyring et al., 2016) (Table 2). Models were selected based on the availability of monthly SST, air-sea heat flux components (shortwave, longwave, sensible, and latent), and surface wind stress data. Historical simulations were retrieved from 1900 onward, until their final date: 2005 for CMIP5 and 2014 for CMIP6. Future projections use high-emissions scenarios: RCP8.5 for CMIP5 (2006–2100) and SSP5-8.5 for CMIP6 (2015–2100). For models with ensembles, only the first member was included.

All simulations were linearly interpolated to a $1° \times 1°$ grid. The " historical" period is defined as the 1900–1925 average, and the "future" as the 2075–2100 average. Future changes (Δ) represent the difference between these two periods. Present-day changes (Δ_{pres}) are calculated as the difference between 2000–2020 and 1980–2000 and can be compared with observed estimates. The MMM is the average across all 63 CMIP5 and CMIP6 simulations.

SST observations were taken from COBE data (Hirahara et al., 2014). To calculate the climatological SST bias (shown in Figure 8), we computed the difference between model SST and COBE observations over the 1900–1925 period. Present-day changes ($\Delta_{pres}T$) for COBE observations are calculated as the difference between 2000–2020 and 1980–2000, consistent with the CMIP model analysis approach.

2.2. Equation for Relative SST Change

To analyze relative SST changes, we adopt and extend the ocean heat budget framework introduced by ZL14. To help readers follow the mathematical development more easily, Table 1 provides a summary of all acronyms and symbols used in this section. ZL14 approach assumes that both present-day and future climates are in approximate equilibrium, such that changes in net surface flux (ΔQ) are balanced by changes in subsurface oceanic processes (ΔO):

$$\Delta Q - \Delta O = 0 \tag{1}$$

Here, ΔO represents the net contribution oceanic processes, including three-dimensional advection (horizontal and vertical), mixing (horizontal and vertical), and entrainment into the surface mixed layer heat budget. These are expressed as equivalent heat fluxes ($W \cdot m^{-2}$). In practice, they diagnose ΔO as $\Delta O = -\Delta Q$.

The total net surface flux ΔQ is composed of:

$$\Delta Q = \Delta SW + \Delta LWD + \Delta LWU + \Delta LH + \Delta SH \tag{2}$$

Table 2
Model List: List of 63 Climate Models From the Coupled Model Intercomparison Project Phase 5 and 6 (CMIP5/6)

Model name	Institute	CMIP
ACCESS1.0	Commonwealth Scientific and Industrial Research Organization, Australia	CMIP5
ACCESS1.3	Commonwealth Scientific and Industrial Research Organization, Australia	CMIP5
ACCESS1-CM2	Commonwealth Scientific and Industrial Research Organization, Australia	CMIP6
ACCESS1-ESM1.5	Commonwealth Scientific and Industrial Research Organization, Australia	CMIP6
AWI-CM-1-1-MR	Alfred Wegener Institute Climate Model, Germany	CMIP6
CAMS-CSM1-0	Chinese Academy of Meteorological Sciences, China	CMIP6
BCC CSM1.1	Beijing Climate Center, China Meteorological Administration, China	CMIP5
BCC CSM1.1(M)	Beijing Climate Center, China Meteorological Administration, China	CMIP5
CanESM2*	Canadian Center for Climate Modeling and Analysis, Canada	CMIP5
CanESM5	Canadian Center for Climate Modeling and Analysis, Canada	CMIP6
CAS-ESM2-0	Chinese Academy of Sciences, China	CMIP6
CCSM4*	National Center for Atmospheric Research, USA	CMIP5
CESM2*	National Center for Atmospheric Research, USA	CMIP6
CESM2-WACCM*	National Center for Atmospheric Research, USA	CMIP6
CIESM*	Department of Earth System Science, China	CMIP6
CMCC-CESM	Centro Euro-Mediterraneo Per I Cambiamenti Climatici, Italy	CMIP5
CMCC-CM	Centro Euro-Mediterraneo Per I Cambiamenti Climatici, Italy	CMIP5
CMCC-CMS	Centro Euro-Mediterraneo Per I Cambiamenti Climatici, Italy	CMIP5
CMCC-CM2-SR5	Centro Euro-Mediterraneo Per I Cambiamenti Climatici, Italy	CMIP6
CMCC-ESM2	Centro Euro-Mediterraneo Per I Cambiamenti Climatici, Italy	CMIP6
CNRM-CM5	Center National de Recherches Météorologiques, France	CMIP5
CNRM-CM6-1	Center National de Recherches Météorologiques, France	CMIP6
CNRM-CM6-1-HR	Center National de Recherches Météorologiques, France	CMIP6
CNRM-ESM2-1	Center National de Recherches Météorologiques, France	CMIP6
CSIRO MK3.6.0	CSIRO and Queensland Climate Change Center of Excellence, Australia	CMIP5
E3SM-1-1*	US Department of Energy, USA	CMIP6
EC-EARTH3-CC	EC-Earth Consortium, Europe	CMIP6
EC-EARTH3	EC-Earth Consortium, Europe	CMIP6
EC-EARTH3-VEG	EC-Earth Consortium, Europe	CMIP6
EC-EARTH3-VEG-LR	EC-Earth Consortium, Europe	CMIP6
FGOALS-f3-L	Chinese Academy of Sciences, China	CMIP6
FGOALS-G3*	Chinese Academy of Sciences, China	CMIP6
FIO-ESM-2-0*	First Institute of Oceanography, China	CMIP6
GFDL-CM3	Geophysical Fluid Dynamics Laboratory, USA	CMIP5
GFDL-CM4	Geophysical Fluid Dynamics Laboratory, USA	CMIP6
GFDL-ESM2G	Geophysical Fluid Dynamics Laboratory, USA	CMIP5
GFDL-ESM2M	Geophysical Fluid Dynamics Laboratory, USA	CMIP5
GFDL-ESM4	Geophysical Fluid Dynamics Laboratory, USA	CMIP6

Table 2
Continued

Model name	Institute	CMIP
INM-CM4*	Institute for Numerical Mathematics, Russia	CMIP5
IPSL-CM5A-LR	Institute Pierre-Simon Laplace, France	CMIP5
IPSL-CM5A-MR	Institute Pierre-Simon Laplace, France	CMIP5
IPSL-CM5B-LR	Institute Pierre-Simon Laplace, France	CMIP5
IPSL-CM6A-LR	Institute Pierre-Simon Laplace, France	CMIP6
KIOST-ESM	Korea Institute of Ocean Science and Technology, Korea	CMIP6
MIROC5	The University of Tokyo, NIES, and JAMSTEC, Japan	CMIP5
MIROC6	The University of Tokyo, NIES, and JAMSTEC, Japan	CMIP6
MIROC-ES2L	The University of Tokyo, NIES, and JAMSTEC, Japan	CMIP5
MIROC-ESM	The University of Tokyo, NIES, and JAMSTEC, Japan	CMIP5
MIROC-ESM-CHEM	The University of Tokyo, NIES, and JAMSTEC, Japan	CMIP5
MPI-ESM-LR	Max Planck Institute for Meteorology, Germany	CMIP5
MPI-ESM-MR	Max Planck Institute for Meteorology, Germany	CMIP5
MPI-ESM1-2-HR	Max Planck Institute for Meteorology, Germany	CMIP6
MPI-ESM1-2-LR	Max Planck Institute for Meteorology, Germany	CMIP6
MRI-CGCM3	Meteorological Research Institute, Japan	CMIP5
MRI-ESM1	Meteorological Research Institute, Japan	CMIP5
MRI-ESM2	Meteorological Research Institute, Japan	CMIP6
NESM3	Nanjing University of Information Science and Technology, China	CMIP6
NordESM1-M	Norwegian Climate Center, Norway	CMIP5
NordESM1-ME*	Norwegian Climate Center, Norway	CMIP5
NordESM2-LM*	Norwegian Climate Center, Norway	CMIP6
NordESM2-MM*	Norwegian Climate Center, Norway	CMIP6
TaiESM1*	Research Center for Environmental Changes, Taiwan	CMIP6
UKESM1-0-LL	Met Office Hadley Center, UK	CMIP6

Note. Models marked with an asterisk (*) indicate missing surface wind components (uas,vas). Model name, research institute, and CMIP phase are provided for each coupled model.

where ΔSW is the changes in net shortwave radiation, ΔLWD and ΔLWU are the changes in downward and upward longwave radiation, and ΔLH and ΔSH are the changes in latent and sensible heat fluxes.

ZL14 then decomposed ΔQ into two parts: a "forcing" component (ΔQ_{For}), independent of local SST changes, and a "feedback" component ($-\alpha\Delta T$), linearly dependent on local SST changes ΔT, with α being the total feedback coefficient. This gives $\Delta Q = \Delta Q_{For} - \alpha\Delta T$.

We briefly summarize how each flux component is treated in ZL14 to derive their equation for ΔT (their Equation 8), so the reader can follow the methodology without referring to the original paper. They first assume ΔSW and ΔLWD to be independent of ΔT, so that they are treated *purely as forcing terms* (i.e., $\alpha_{SW} = \alpha_{LWD} = 0$). Governed by the Stefan–Boltzmann law, ΔLWU is entirely considered as a feedback term: $\Delta LWU = -\alpha_{LWU}\Delta T$, where $\alpha_{LWU} = 4\sigma[T]^3$, with σ the Stefan-Boltzmann constant and **[T]** the present-day SST. The decomposition of latent heat flux is based on the Clausius–Clapeyron relationship, separating SST-driven evaporation from other factors: $\Delta LH = \Delta LH_{For} - \alpha_{LH}\Delta T$, with $\alpha_{LH} = \gamma_1[LH]$. Here **[LH]** is the present-day latent heat flux and $\gamma_1 = 0.06\ K^{-1}$ is a constant derived from the Clausius-Clapeyron equation and representative of tropical oceans. The feedback term $-\alpha_{LH}\Delta T$ represents the Newtonian cooling feedback, where warmer SST enhances evaporation, damping further warming, while ΔLH_{For} accounts for the LH changes related to changes in wind speed, relative humidity, and air-sea temperature difference that are not directly tied to ΔT. ΔSH is similarly expressed as

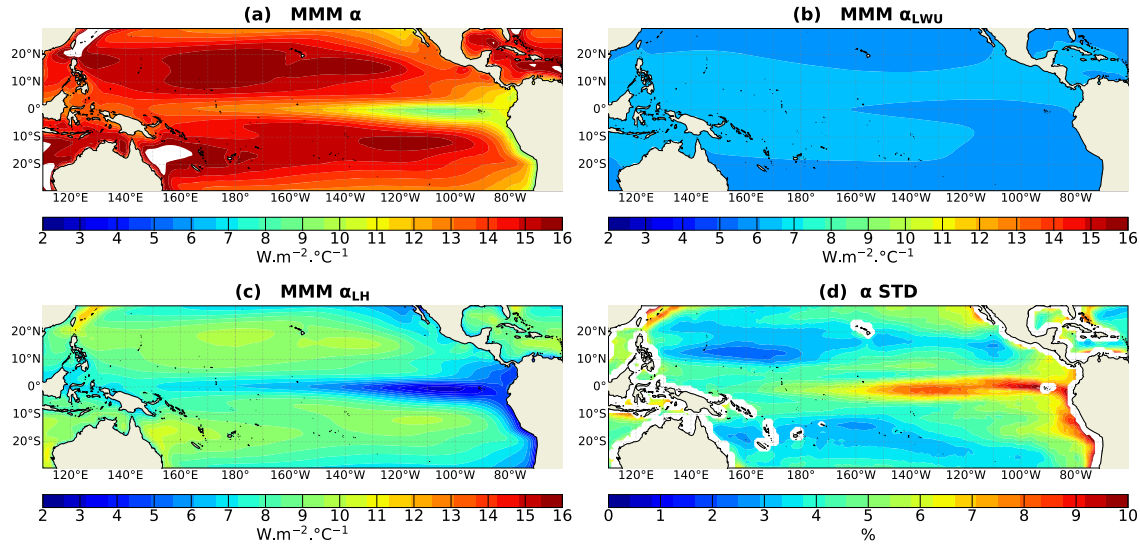

Figure 2. Coupled Model Intercomparison Project multi-model mean (MMM) air-sea fluxes feedback total coefficient and their components: (a) Total coefficient (**α**), with contributions from: (b) latent heat flux feedback ($\boldsymbol{\alpha_{LWU}}$) and (c) upward longwave radiation ($\boldsymbol{\alpha_{LH}}$) feedback in W/m^2/°C. (d) Inter-model standard deviation of **α**, expressed as a percentage of the MMM.

$\Delta SH = \Delta SH_{For} - \alpha_{SH}\Delta T$, where $\alpha_{SH} = \gamma_2[V]$. Here **[V]** is the present-day surface wind speed and γ_2 is a coefficient that captures the efficiency of sensible heat transfer.

Substituting all component expressions into Equation 2, ZL14 obtain the following equation ΔQ:

$$\Delta Q = \Delta SW + \Delta LWD - \alpha_{LWU}\Delta T + \Delta LH_{For} - \alpha_{LH}\Delta T + \Delta SH_{For} - \alpha_{SH}\Delta T \quad (3)$$

Rearranging and solving ΔT using Equation 1, ZL14 obtain:

$$\Delta T = \frac{\Delta SW + \Delta LWD + \Delta SH_{For} + \Delta LH_{For} + \Delta O}{4\sigma[T]^3 + \gamma_1[LH] + \gamma_2[V]} \quad (4)$$

In this study, we exclude the SH feedback term. This is justified because under the linearized formulation of LH, we assume no change in the air–sea temperature difference, leading to negligible SST-driven **SH** flux changes. Moreover, this term is found to be extremely small in our calculation (not shown). We will continue to denote ΔSH_{For} as ΔSH.

Defining the total feedback coefficient $\alpha = 4\sigma[T]^3 + \gamma_1[LH]$ and the SST-independent forcing term $\Delta Q_{For} = \Delta SW + \Delta LWD + \Delta SH + \Delta LH_{For}$, **ΔT** equation can then be compactly written as:

$$\Delta T = \frac{\Delta Q_{For} + \Delta O}{\alpha} \quad (5)$$

Figure 2 shows the spatial distribution of surface heat flux feedback coefficients in the tropical Pacific. The latent flux negative feedback α_{LH} (Figure 2c) dominates both the magnitude and spatial structure of the total feedback coefficient α (Figure 2a). While α_{LWU} contributes nearly uniformly across the region (Figure 2b), it primarily serve to elevate the baseline value of α rather than to shape its spatial structure. The spatial pattern of α_{LH} reflects Clausius–Clapeyron effects, with stronger evaporative cooling in regions of higher SST and/or stronger winds. This results in a α_{LH} spatial pattern that closely follow historical SST and wind patterns (not shown). Figure 2d shows the inter-model standard deviation of α, expressed as a percentage of the MMM value. The inter-model spread in **α** is generally modest—less than 5% of the MMM across most of the tropical Pacific. However, this spread increases in the EEP and along the South American coast, where it can reach up to 10%.

To derive an equation for relative SST changes ($\Delta T'$), we apply Reynolds decomposition to Equation 5 which separates each variable into a tropical mean (denoted by an overbar) and a deviation from this mean (denoted by a prime):

$$\overline{\Delta T} + \Delta T' = \frac{\Delta Q_{For}{}' + \overline{\Delta Q_{For}} + \Delta O' + \overline{\Delta O}}{\alpha' + \overline{\alpha}} \tag{5a}$$

Here, $\Delta T'$ represents the change in relative SST, that is the local SST change relative to the tropical mean. We consistently use T' to denote relative SST and $\Delta T'$ for its change.

Rewriting Equation 5a in expanded form:

$$\overline{\alpha}\overline{\Delta T} + \overline{\alpha}\Delta T' + \alpha'\overline{\Delta T} + \alpha'\Delta T' = \overline{\Delta Q_{For}} + \Delta Q_{For}{}' + \overline{\Delta O} + \Delta O' \tag{5b}$$

Averaging Equation 5b over the tropics yields:

$$\overline{\alpha}\overline{\Delta T} = \overline{\Delta Q_{For}} + \overline{\Delta O} - \overline{\alpha'\Delta T'} \tag{6a}$$

We find the cross term $\overline{\alpha'\Delta T'}$ to be negligible (not shown), which simplifies the tropical mean SST response to:

$$\overline{\alpha}\overline{\Delta T} = \overline{\Delta Q_{For}} + \overline{\Delta O} \tag{6b}$$

To isolate $\Delta T'$, we subtract Equation 6b from Equation 5b and retain leading-order terms, verifying that $\Delta T'\alpha'$ is small:

$$\Delta T' = \frac{\Delta Q_{For}{}' + \Delta O' - \alpha'\overline{\Delta T}}{\overline{\alpha}} \tag{7a}$$

Given the limited $\overline{\alpha}$ inter-model diversity (Figure 2d), we approximate it using the MMM $< \overline{\boldsymbol{\alpha}} >$, leading to simplified expression:

$$\Delta T' = \frac{\Delta Q_{For}{}' + \Delta O' - \alpha'\overline{\Delta T}}{\langle \alpha \rangle} \tag{7b}$$

where $\alpha'\overline{\Delta T}$ captures how the spatial inhomogeneity in the feedback coefficient (e.g., weaker evaporative cooling in climatologically cooler regions) shape $\Delta T'$, an effect discussed in Xie et al. (2010).

To validate the use of $< \overline{\alpha} >$, we compare $\Delta T'$ computed using each model's own $\overline{\alpha}$ (Equation 7a) against that computed with MMM $< \overline{\alpha} >$ (Equation 7b). As shown in Figure S1 in Supporting Information S1, the spatial patterns of $\Delta T'$ are nearly identical, with very high correlation coefficients (ranging from 0.990 to 0.997) and regression slopes near unity ($R^2 = 0.960$–1.044) across key tropical regions. This confirms that replacing model-specific $\overline{\boldsymbol{\alpha}}$ with MMM $< \overline{\boldsymbol{\alpha}} >$ values introduce negligible errors (Figure 1a).

For clarity, we denote all terms in the numerator of Equation 7b, when normalized by the feedback coefficient $\langle \boldsymbol{\alpha} \rangle$, with a star superscript (*). Note that in all figures, $\alpha'\overline{\Delta T}^* = \frac{-\alpha'\overline{\Delta T}}{\langle \alpha \rangle}$, with the negative sign already incorporated for ease of interpretation in figures.

To quantify the contribution of each process to inter-model diversity in $\Delta T'$, we decompose its variance by expressing it as the sum of covariances between $\Delta T'$ and each term in the right-hand side of Equation 7b:

$$\mathrm{Var}(\Delta T') = \mathrm{Cov}\left(\Delta T', \Delta Q_{For}{}'^*\right) + \mathrm{Cov}\left(\Delta T', \Delta O'^*\right) + \mathrm{Cov}\left(\Delta T', \alpha'\overline{\Delta T}^*\right) \tag{8}$$

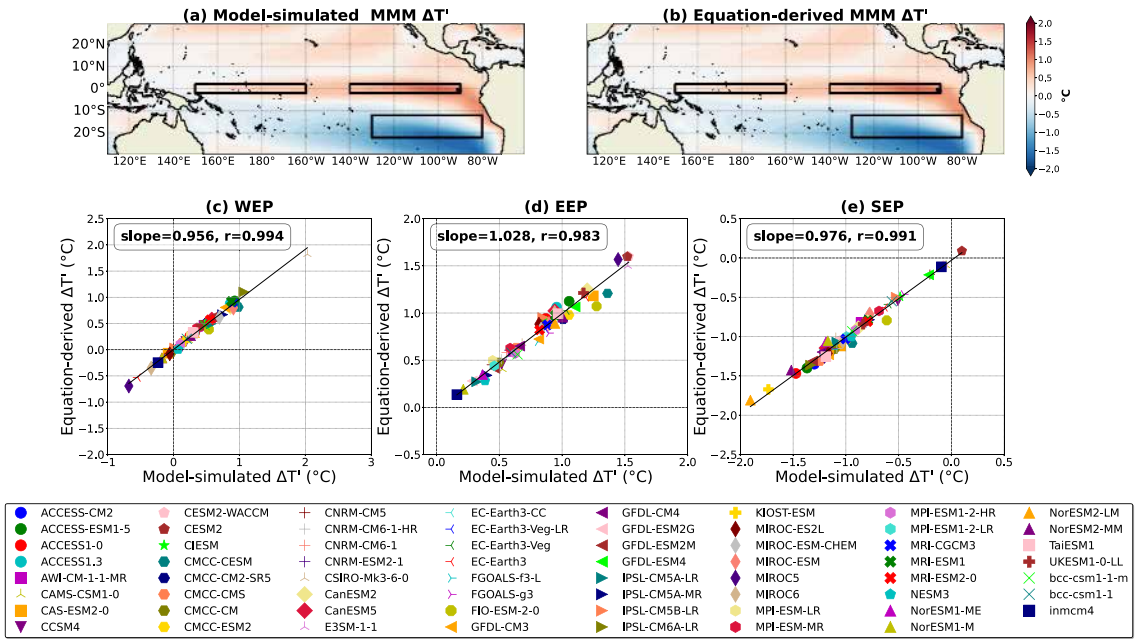

Figure 3. Validation of the reconstructed relative SST change $\Delta T'$: (a) Coupled Model Intercomparison Project (CMIP) multi-model mean (MMM $\Delta T'$) directly from model outputs and (b) reconstructed MMM $\Delta T'$ using Equation 7b. Scatterplots comparing reconstructed versus model-simulated $\Delta T'$ across individual CMIP models for three key regions outlined in panels (a) and (b): (c) Western Equatorial Pacific, (d) Eastern Equatorial Pacific and (e) Southeastern Pacific. Each symbol represents one CMIP model. Black lines in panels (c)–(e) indicates the best-fit linear regression. Correlation and regression coefficients (both significant at 95% confidence level) are shown in the upper right of each panel.

This decomposition allows assessing how each process contributes to the overall spread in $\Delta T'$ across models. A positive covariance indicates that a component amplifies $\Delta T'$ inter-model diversity (i.e., positively contributing to variance), while a negative covariance indicates that a component decreases $\Delta T'$ inter-model diversity. This approach has been widely in climate science to assess the relative role of different physical drivers in temperature variance growth or decay and to diagnose positive or negative feedback mechanisms (e.g., Guan et al., 2019; Guan & McPhaden, 2016; Takahashi et al., 2023). In a CMIP context, more closely aligned with our objective, Kent et al., 2015 employed a similar approach to identify key contributors to uncertainties in projected seasonal tropical precipitation. Thus, this framework provides a systematic and interpretable means of attributing inter-model spread in tropical Pacific warming patterns to distinct physical processes.

We focus on three regions characterized by significant inter-model diversity (Figure 1b): the western equatorial Pacific (WEP; 2°N–2°S, 150°E−160°W), the eastern equatorial Pacific (EEP; 2°N–2°S, 140°W–90°W), and the southeastern Pacific (SEP; 12°S–22°S, 80°W–130°W). Figure 3 demonstrates that Equation 7b effectively reproduces the MMM $\Delta T'$ pattern (Figures 3a and 3b), as well as the inter-model $\Delta T'$ diversity in all three focus regions, with correlations exceeding 0.98.

Figure S2 in Supporting Information S1 compares the total inter-model variance of $\Delta T'$, computed directly from the ensemble, with the sum of covariances derived from the three components in Equation 8. The perfect agreement confirms that our decomposition approach accurately and fully accounts for the inter-model spread of $\Delta T'$ across all focus regions.

3. Drivers of the MMM Projected Relative SST Changes

Figure 4 illustrates the contributions of individual processes to the MMM relative SST change ($\Delta T'$), calculated using Equation 7b. Consistent with ZL14, the spatial variation in the feedback coefficient ($\alpha' \overline{\Delta T}^*$) emerges as the primary driver of the MMM El Niño-like warming in the equatorial Pacific. Additionally, $\Delta LWD'^*$ slightly amplifies the equatorial warming. In contrast, $\Delta SW'^*$ mitigates warming in the WEP, while $\Delta LH'^*_{For}$ reduces warming in the EEP and strongly contributes to SEP cooling. Ocean processes ($\Delta O'^*$) slightly enhance WEP

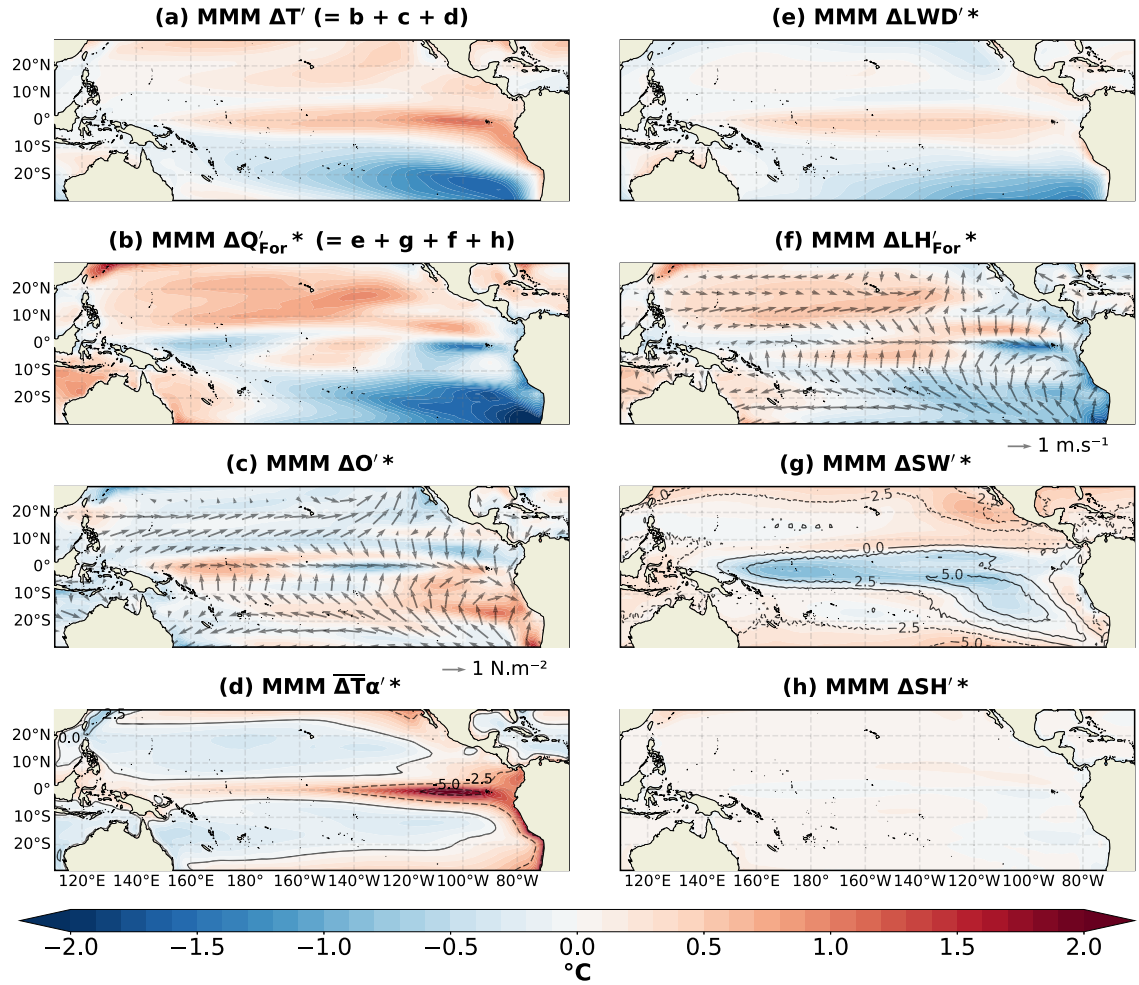

Figure 4. Mechanisms driving the projected multi-model mean (MMM) $\Delta T'$: (a) MMM $\Delta T'$ (°C), decomposed into contributions (shading in °C) from: (b) total surface heat flux forcing ($\Delta Q_{For}{}'*$), (c) ocean dynamics ($\Delta O'*$, with MMM wind-stress changes in N.m^{-2} shown as vectors) and (d) feedback coefficient inhomogeneity ($\alpha'\overline{\Delta T}*$, with MMM relative total feedback coefficient alpha in W.m^{-2}. °C^{-1} as contours). $\Delta Q_{For}{}'*$) is further decomposed into individual components: (e) net longwave ($\Delta LWD'*$), (f) latent forcing ($\Delta LH'_{For}*$, with MMM relative wind speed change in m.s^{-1} as contours), (g) shortwave radiation ($\Delta SW'*$, with MMM cloud cover changes in % as contours) and (h) sensible heat flux ($\Delta SH'*$). Note: by construction, the reconstructed MMM $\Delta T'$ satisfies $\Delta T' = \Delta O'* + \alpha'\overline{\Delta T}* + \Delta Q_{For}{}'*$ (panels a = b + c + d) and $\Delta Q_{For}{}'*$ satisfies $\Delta Q_{For}{}'* = \Delta LWD'* + \Delta LH'_{For}* + \Delta SW'* + \Delta SH'*$ (panel b = e + f + g + h).

warming and partially offset warming in the EEP. Overall, these findings emphasize the dominant role of feedback coefficient inhomogeneity in shaping MMM equatorial $\Delta T'$, with latent heat flux forcing playing a key role in driving SEP cooling.

Figure 5 provides a quantitative breakdown from individual processes to $\Delta T'$ in the three targeted regions. Consistent with Figure 4, the MMM relative cooling in the SEP ($\sim -1\,°C$) is primarily driven by the SST-independent component of the surface net heat flux change ($\Delta Q_{For}{}'*$). Within $\Delta Q_{For}{}'*$, $\Delta LH'_{For}*$ and $\Delta LWD'*$ together play the leading role in driving the cooling, while $\Delta SW'*$ and $\Delta SH'*$ have negligible effects. $\Delta O'*$ slightly counteract the cooling, and $\alpha'\overline{\Delta T}*$ has a minimal effect (Figure 5a). In the WEP, the modest MMM relative warming (~0.3°C) is equally driven by $\Delta O'*$ and $\alpha'\overline{\Delta T}*$, while $\Delta Q_{For}{}'*$ acts as a counterbalance, primarily through $\Delta SW'*$ cooling linked to increased cloud cover (Figures 4b and 4c and 5b). In the EEP, the larger MMM relative warming is mainly driven by $\alpha'\overline{\Delta T}*$, with $\Delta Q_{For}{}'*$ and $\Delta O'*$ providing a damping effect (Figure 5c). Within $\Delta Q_{For}{}'*$, both $\Delta LH'_{For}*$ and $\Delta SW'*$ are significant contributors. Overall, the reduction in the equatorial $\Delta T'$ gradient is driven by $\alpha'\overline{\Delta T}*$ and slightly dampened by $\Delta O'*$, with $\Delta Q_{For}{}'*$ having a negligible impact (Figure 5d).

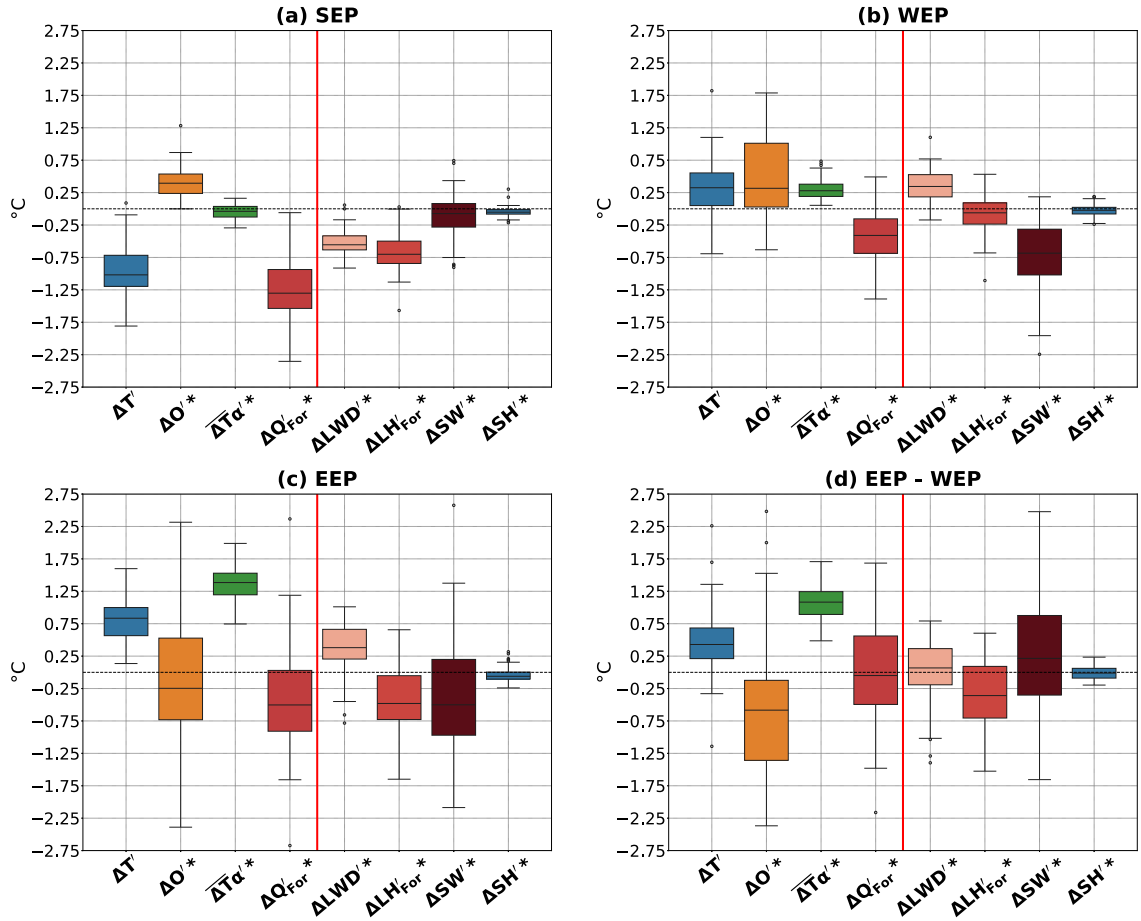

Figure 5. Mechanisms driving projected multi-model mean (MMM) $\Delta T'$ in selected tropical Pacific regions. MMM $\Delta T'$ and contributing components (as defined in Equation 7b) are shown for (a) Southeastern Pacific, (b) Western Equatorial Pacific (WEP), (c) Eastern Equatorial Pacific (EEP) and (d) EEP minus WEP. Each panel includes the contributions from ocean dynamics ($\Delta O'$*), feedback coefficient inhomogeneity ($\alpha' \overline{\Delta T}$*) and atmospheric forcing ($\Delta Q_{For}{}'$*) further broken down into: longwave ($\Delta LW'_{For}$*), latent ($\Delta LH'_{For}$*), shortwave ($\Delta SW'$*) and sensible ($\Delta SH'$*) heat fluxes.

This section demonstrates that the MMM SEP relative cooling is primarily driven by atmospheric forcing, specifically through intensified evaporative cooling due to increased wind speeds and reduced downward longwave radiation. Conversely, the MMM El Niño-like warming is largely attributed to the spatial inhomogeneity of the feedback coefficient. The next section explores the factors driving the inter-model spread of $\Delta T'$ in the three targeted regions.

4. Drivers of Inter-Model Projected Relative SST Diversity

The SEP exhibits a wide range of inter-model relative $\Delta T'$ cooling, spanning from 0 to −2°C (Figure 5a). Variance decomposition reveals that $\Delta T'$ diversity in this region is predominantly driven by $\Delta Q_{For}{}'$* (Figure 6a), with only a minor offsetting contribution from $\Delta O'$*. Within $\Delta Q_{For}{}'$*, $\Delta LH'_{For}$* and $\Delta SW'$* contribute equally, each accounting for 42%, followed by $\Delta LWD'$* at 32%. $\Delta SH'$* plays a negligible role. The magnitude of cooling associated with $\Delta LH'_{For}$* is strongly correlated with wind speed intensification across models ($r = -0.819$, Figure 6b). Similarly, the spread in $\Delta SW'$* is strongly influenced by variations in cloud cover changes ($r = 0.717$; Figure 6c).

The equatorial Pacific also exhibits significant inter-model $\Delta T'$ diversity (Figure 1b), particularly in the WEP, where $\Delta T'$ ranges from −0.7 to 1°C (Figures 5b and 5c). Variance decomposition (Figures 7a–7c) identifies $\Delta O'$ as the primary driver of $\Delta T'$ diversity, contributing 108% in the WEP, 130% in the EEP and 172% for the equatorial

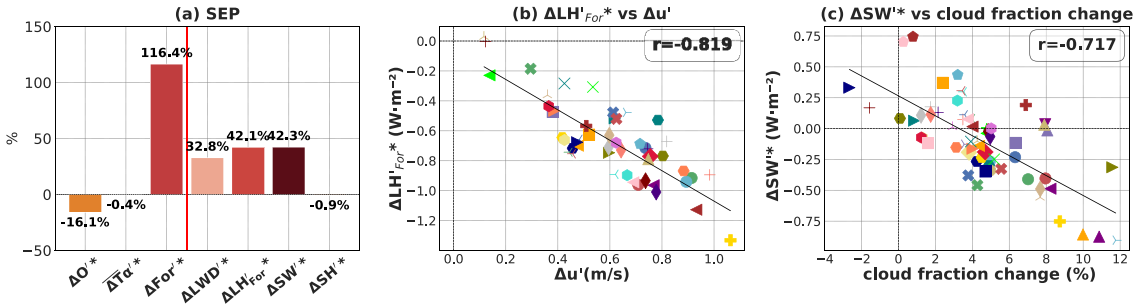

Figure 6. Drivers of $\Delta T'$ inter-model diversity in the SEP: (a) Decomposition of inter-model variance in Southeastern Pacific (SEP) $\Delta T'$ using Equation 8. Contributions are shown for: ocean dynamics ($\Delta O'^*$), feedback coefficient inhomogeneity ($\alpha' \overline{\Delta T}^*$) and atmospheric forcing ($\Delta Q_{For}{}'^*$), with the latter further divided into: longwave radiation ($\Delta LWD'^*$), latent heat flux ($\Delta LH'_{For}{}^*$), shortwave radiation ($\Delta SW'^*$) and sensible heat flux ($\Delta SH'^*$). The vertical red line separates the main contributors to total variance (left, summing to 100%) from the detailed breakdown of $\Delta Q_{For}{}'^*$ component (right, which sum to the $\Delta Q_{For}{}'^*$ contribution shown on the left). Scatterplots of (b) $\Delta LH'_{For}{}^*$ versus wind speed changes $\Delta u'$, and (c) $\Delta SW'^*$ changes versus cloud fraction changes averaged across Coupled Model Intercomparison Project models both averaged over the SEP box. Correlation coefficients (significant at the 95% confidence level) are indicated in the upper right corner of each panel.

gradient. This dominance is highlighted by strong correlations between $\Delta O'^*$ and $\Delta T'$ (Figures 7d–7f), particularly in the WEP ($r = 0.769$) and for the equatorial gradient ($r = 0.804$). While the correlation is weaker in the EEP ($r = 0.48$), it remains significant. The higher correlation in the WEP suggests a potentially important role of oceanic processes in this region. Feedback coefficient inhomogeneity contributes modestly (12% in the WEP and 21% in the EEP) but has no impact on the equatorial gradient. Net heat flux forcing consistently reduces $\Delta T'$ diversity, with $\Delta SW'^*$ as the primary damping factor across all regions, and latent forcing playing a notable role in the WEP.

Our results indicate a key role of oceanic processes in modulating the westward extension of the warming and changes in the zonal SST gradient. However, the factors driving $\Delta O'^*$ diversity remain unclear. The MMM zonal wind-stress response shows weakened trade winds across the equatorial Pacific, consistent with a weaker Walker Circulation (Figure 8a). Inter-model correlations between $\Delta O'^*$ and local wind stress changes are significant in both the western ($r = 0.634$) and eastern Pacific ($r = 0.44$), at the 95% confidence level (Figures 8b and 8c). The positive correlations align with the expectation that greater trade wind relaxation reduces upwelling, leading to more warming. Surprisingly, the correlation is stronger in the western Pacific than in the eastern Pacific, where upwelling is observed. This may be linked to changes in the westward extension of the south equatorial current in response to wind changes, which could amplify warming signals in the western Pacific through horizontal advection processes.

The cold tongue bias, a common feature of most CMIP models (Figure 8d), has been suggested to influence the projected warming pattern in the tropical Pacific (Li et al., 2016). This bias, associated with an overly vigorous equatorial upwelling, may amplify the ocean thermostat effect under global warming (Clement et al., 1996; DiNezio et al., 2009; Ying et al., 2019). To assess this, we examine the relationship between $\Delta O'^*$ and the historical cold tongue bias (Figures 8e and 8f), finding a significant correlation ($r = 0.497$, 95% confidence) in the EEP. This finding supports the idea that stronger upwelling and a more pronounced cold tongue bias in the eastern Pacific enhance cooling by oceanic processes there, reducing the El Niño like warming. An identical analysis was conducted using a more recent period for SST bias calculations (1960–1980, Figure S3 in Supporting Information S1), yielding similar results to those obtained with the initial 1900–1925 period, confirming that our conclusions are robust regardless of the reference period.

Our findings reveal that the MMM El Niño-like warming and the associated reduction in the equatorial SST gradient are primarily driven by differential evaporative cooling. In contrast, oceanic processes predominantly control the inter-model diversity in the westward extent of the warming and changes in the zonal SST gradient. Correlations with zonal wind stress changes and the historical cold tongue biases suggest that these oceanic processes result from a combination of wind-driven responses and the ocean dynamical thermostat mechanism. In the western Pacific, reduced trade winds lead to greater warming, potentially through zonal advection associated with changes in equatorial currents and vertical processes linked to the unrealistically westward-extended cold tongue in CMIP models. In the eastern Pacific, a stronger cold tongue bias and enhanced vertical upwelling amplify the ocean thermostat, counteracting the El Niño-like warming pattern induced by the trade wind relaxation.

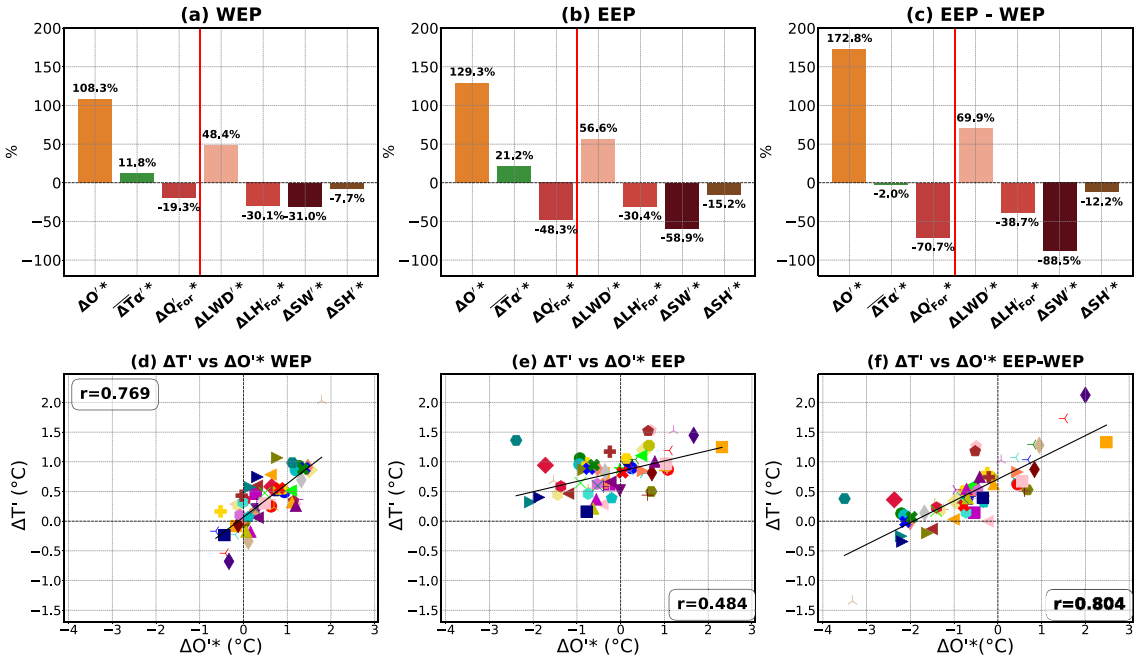

Figure 7. Drivers of $\Delta T'$ inter-model diversity at the equator: (a)-(c) Decomposition of $\Delta T'$ inter-model variance using Equation 8 for: (a) Western Equatorial Pacific (WEP), (b) Eastern Equatorial Pacific (EEP) and (c) the equatorial SST gradient. Contributions are shown for: ocean dynamics ($\Delta O'^*$), feedback inhomogeneity ($\alpha' \overline{\Delta T}^*$) and atmospheric forcing ($\Delta Q_{For}'^*$) which is further divided into: longwave radiation ($\Delta LWD'^*$), latent heat flux ($\Delta LH'_{For}*$), shortwave radiation ($\Delta SW'^*$) and sensible heat flux ($\Delta SH'^*$). The vertical red line separates the main contributors to total variance (left, summing to 100%) from the detailed breakdown of $\Delta Q_{For}'^*$ component (right, which sum to the $\Delta Q_{For}'^*$ contribution shown on the left). Scatterplots of $\Delta T'$ versus $\Delta O'^*$ in the: (d) WEP, (e) EEP and (f) equatorial SST gradient. Correlation coefficients (significant at the 95% confidence level) are indicated in the upper right corner of each panel.

5. Present-Day Period

So far, this study has explored on the mechanisms shaping the TPWP in future projections. We now shift focus to the present-day period to address discrepancies between observed and modeled changes. As highlighted in the introduction, observations indicated a $\Delta T'$ cooling in the central and eastern Pacific over recent decades (Figure 9a), whereas the MMM indicates warming (Figure 9b). To investigate this divergence, we first assess whether the mechanisms identified for future projections also hold for the present-day period, concentrating on the equatorial region, where the disagreement is most pronounced.

Figures 10a and 10b illustrates the mechanisms driving MMM $\Delta_{pres}T'$ in the WEP and EEP during the present-day period. The processes are qualitatively consistent with those identified for future projections. Evaporative feedback heterogeneity remains the dominant factor shaping the El Niño-like pattern, with oceanic processes contributing notably in the western Pacific. Inter-model diversity in both regions is primarily driven by $\Delta_{pres}O'^*$, mirroring in future scenarios. The same mechanisms explain MMM equatorial warming and its diversity during both present-day and future periods, including for the zonal $\Delta_{pres}T'$ gradient (not shown).

Figure 11 examines the mechanisms behind EEP $\Delta T'$ during the present-day period, with models ordered from the largest relative warming to the largest relative cooling. The 10 models showing the most pronounced EEP cooling all simulate weaker cooling than observed (Figure 11b; Figure 9c shows the mean of these "coolest" models). These models also tend to simulate a weaker future EEP warming compared to other models (0.45°C vs. 0.97°C). This aligns with the idea that TPWP influences transient climate sensitivity (e.g., Stevens et al., 2016; Watanabe et al., 2024). The mechanisms driving EEP cooling in these "coolest" models are now explored.

Figure 12 shows a scatterplot of $\Delta_{pres}Q_{For}'^*$ versus $\Delta_{pres}O'^*$ for the present-day period. Models capturing best observed cooling must fall sufficiently below and to the left of the y = -x line, where the combined effects of forcing and oceanic processes counteract the warming from feedback heterogeneity (Figure 11d). Among the 10 models matching observations most closely, the cooling mechanisms vary considerably: in 3 models, $\Delta_{pres}O'^*$

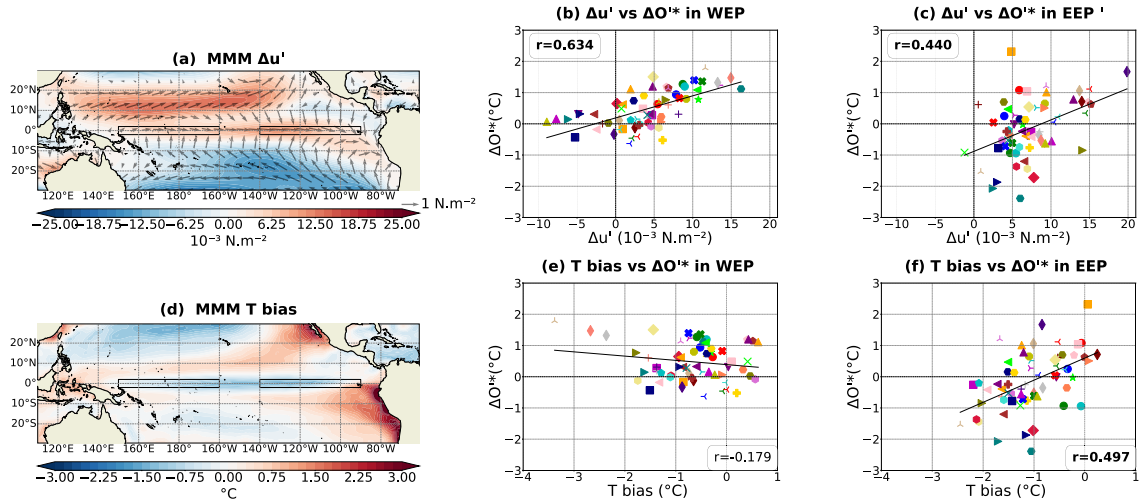

Figure 8. Drivers of $\Delta O'$ inter-model diversity at the equator. (a) multi-model mean (MMM) zonal wind stress change $\Delta u'$ and (d) MMM historical SST bias, calculated as the difference between MMM and COBE SST data for the 1900–1925 period. Scatterplots showing the relationship between $\Delta O'^*$ and zonal wind stress change $\Delta u'$ averaged over (b) the Western Equatorial Pacific (WEP) and (c) the Eastern Equatorial Pacific (EEP), respectively. Scatterplots showing the relationship between $\Delta O'^*$ and historical SST bias, averaged over (e) WEP and (f) EEP, respectively. Correlation coefficients (significant at the 95% confidence level) are indicated in each panel.

alone drives cooling, in 2 models, $\Delta_{pres}Q_{For}{}'^*$ dominates; and, in the remaining five, a both flux forcing and oceanic processes contribute. The dominant components of $\Delta_{pres}Q_{For}{}'^*$ also differ, with clouds driving cooling in some models and wind changes in others (not shown). This analysis underscores that agreement with observed cooling arises from diverse mechanisms across models. The variability in contributing processes complicates efforts to reconcile CMIP simulations with observations, highlighting the need for further investigation into the drivers of present-day TPWP trends.

6. Summary and Discussion

This study investigates the TPWP projected by CMIP models, focusing on the El Niño-like warming pattern (enhanced warming in the eastern Pacific) and reduced warming in the SEP. Although these features dominate the multi-model-mean (MMM), individual models show significant deviations, underscoring the need to understand the underlying mechanisms. Using an heat budget framework adapted from Zhang and Li (2014), we analyze the drivers of the relative SST (SST minus its tropical mean) changes in 22 CMIP5 and 31 CMIP6 models to elucidate the processes driving both the MMM warming pattern and inter-model diversity, for both future projections and the present-day period.

Our results show that the SEP relative cooling and its inter-model diversity are primarily driven by heat flux forcing. Consistent with Xie et al. (2010), we find that this cooling is associated with enhanced evaporation caused by strengthened trade winds, which have been related to the poleward expansion of the Southern Hemisphere Hadley Cell (Grise et al., 2019; Jebri et al., 2020; Power et al., 2021). We further demonstrate that inter-model differences in the magnitude of relative cooling are closely tied to variations in trade wind intensification and the associated evaporation. While the trade wind strengthening is a robust signal supported by observations (Power et al., 2021), its intensity varies significantly across models. This variability arises from differing representations of Hadley Cell expansion mechanisms. In particular, climate sensitivity explains a large portion of the expansion variance, while residual differences are linked to variations in meridional SST gradients: models with stronger Southern Hemisphere gradients tend to exhibit greater trade wind intensification (Grise & Polvani, 2016; Liu & Alexander, 2007). Additionally, processes in the Southern Ocean (including sea ice dynamics and cloud feedbacks) modulate the subtropical high-pressure systems that drive trade winds (Jebri et al., 2020). Finally, regional stratocumulus cloud responses further influence shortwave radiation changes, potentially amplifying or dampening the cooling effect in this region (Lin et al., 2014).

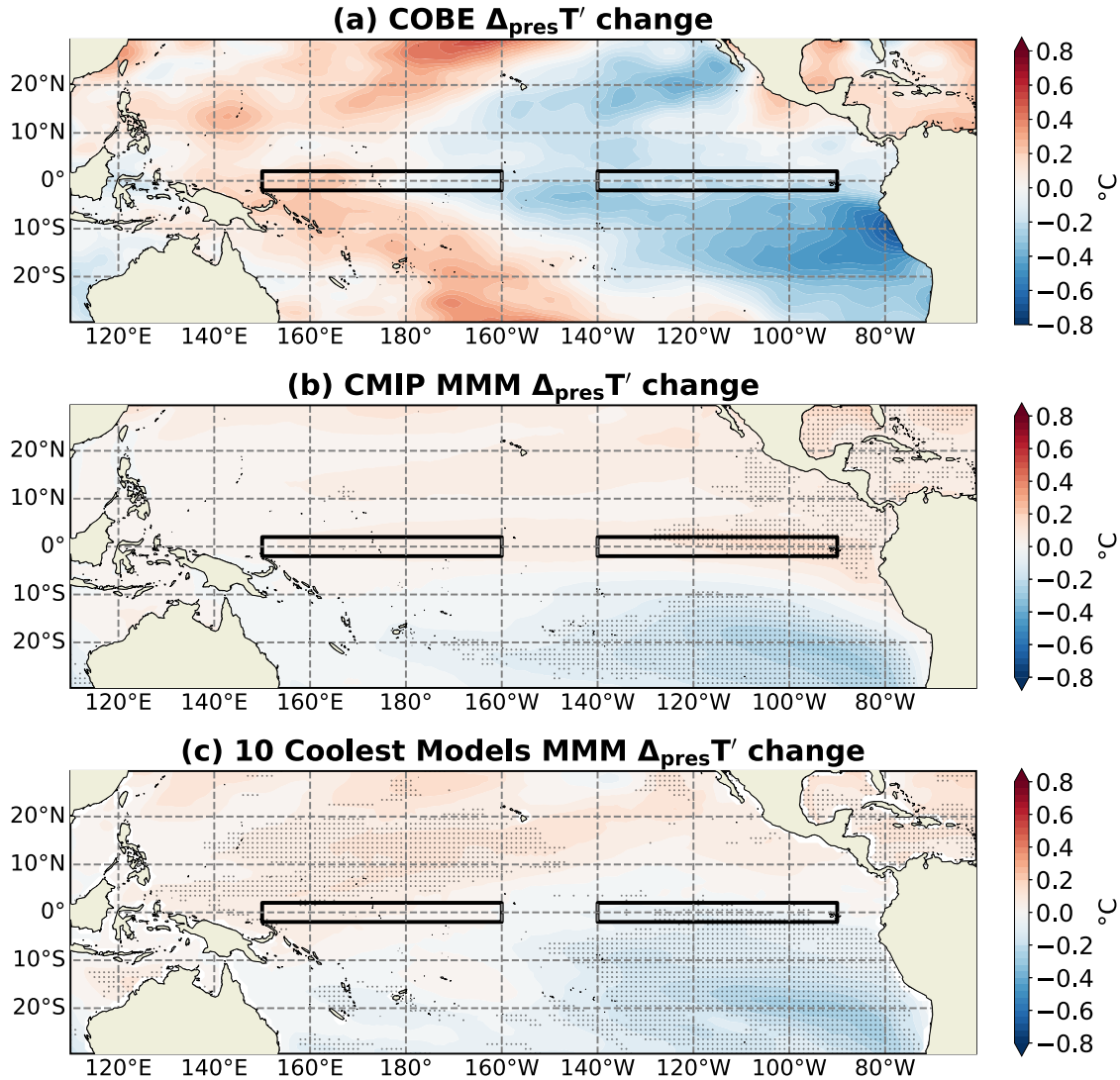

Figure 9. Present-day tropical Pacific warming pattern (1980–2020): relative SST change ($\Delta_{pres}T'$), calculated as the difference between 2000–2020 and 1980–2000 periods for: (a) observations (COBE) and (b) Coupled Model Intercomparison Project multi-model mean and (c) the average of the 10 models showing the strongest cooling in the Eastern Equatorial Pacific (2°N–2°S, 140–90°W). In panels (b) and (c), dotted regions indicate area where at least 75% of models agree on the sign of the change.

Consistent with prior studies (Fu & Fedorov, 2023; Heede et al., 2020; S. P. Xie et al., 2010; Zhang & Li, 2014), our results confirm that differential evaporative cooling drives the MMM El Niño-like warming pattern. Oceanic processes moderate this warming in the EEP, consistent with the ocean thermostat mechanism. However, inter-model diversity in equatorial warming is primarily controlled by variations in ocean processes. These supports findings by Park et al. (2022) but contrast with Ying and Huang (2016), who emphasized cloud–radiation feedback as the dominant driver. In our analysis, cloud–radiation feedback systematically reduces inter-model spread, counteracting the effects of ocean processes variability.

In this study, we have treated CMIP5 and CMIP6 models as a combined ensemble. Nonethless, it is important to assess whether our main findings hold across model generation. Both CMIP5 and CMIP6 broadly exhibit similar patterns of inter-model diversity in the tropical Pacific (Figure S4 in Supporting Information S1). However, there are notable differences in regional behavior. In the WEP, CMIP6 models show greater consensus compared to CMIP5, yet oceanic processes remain the dominant source of model diversity for both generations (Figure S5 in Supporting Information S1). In contrast, inter-model spread in the SEP is markedly greater in CMIP6 (Figure S4 in Supporting Information S1). Additionally, the dominant atmospheric driver of this diversity shifts from latent

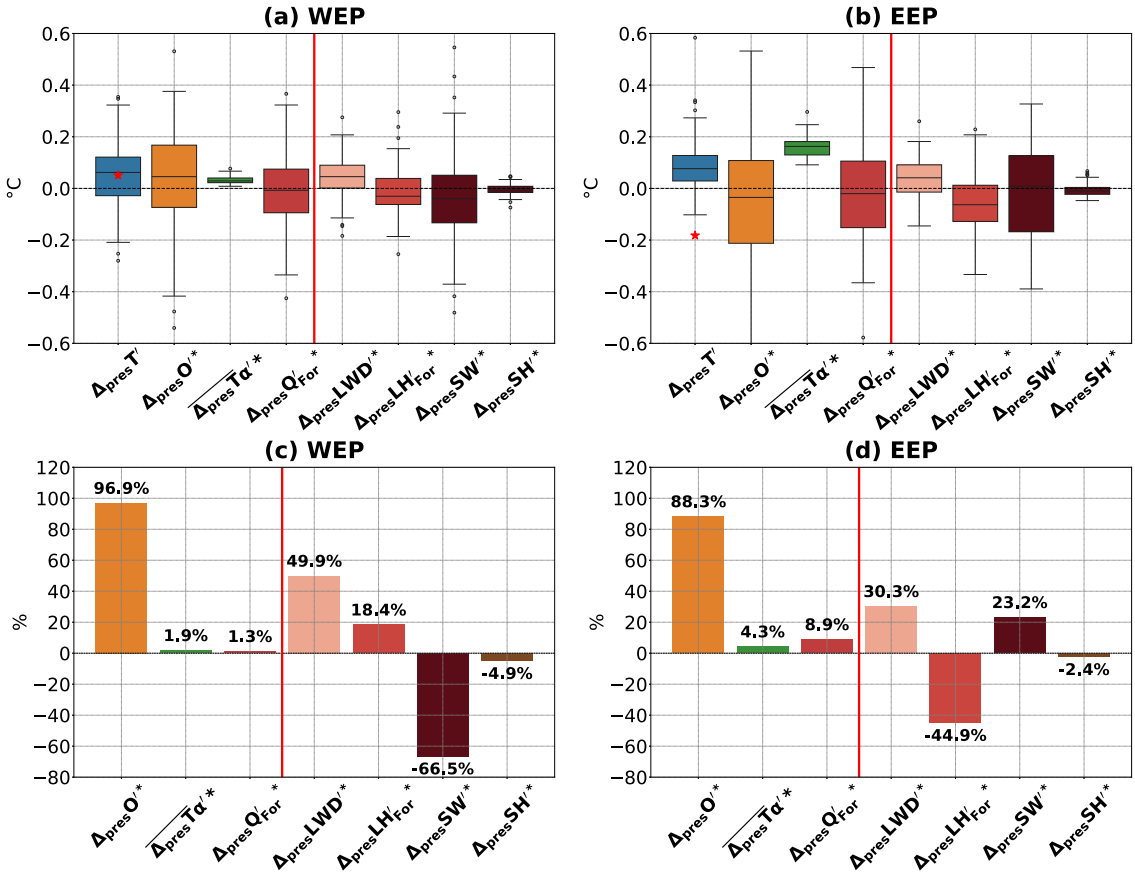

Figure 10. Drivers of present-day MMM $\Delta_{pres}T'$ and its inter-model diversity at the equator. (a),(b) multi-model mean $\Delta_{pres}T'$ in the Western Equatorial Pacific (WEP) and Eastern Equatorial Pacific (EEP), along with contributions based on Equation 7b from: oceanic processes ($\Delta_{pres}O'^*$), feedback coefficient inhomogeneity ($\overline{\alpha' \Delta_{pres}T}^*$) and atmospheric forcing ($\Delta_{pres}Q_{For}{}'^*$), which is further decomposed into longwave radiation ($\Delta_{pres}LWD'^*$), latent heat flux ($\Delta_{pres}LH'_{For}{}^*$), shortwave radiation ($\Delta_{pres}SW'^*$) and sensible heat flux ($\Delta_{pres}SH'^*$). The red star denotes the observed $\Delta_{pres}T'$ from COBE data. (c),(d) Decomposition of inter-model variance in $\Delta_{pres}T'$ for WEP and EEP, using Equation 5b. Contributions from the same components as in panels (a) and (b) are shown. The vertical red line separates the main contributors to total variance (left, summing to 100%) from the detailed breakdown of $\Delta_{pres}Q_{For}{}'^*$ component (right, which sum to the $\Delta Q_{For}{}'^*$ contribution shown on the left).

heat fluxes in CMIP5 to shortwave radiation in CMIP6 (Figure S5 in Supporting Information S1). These findings emphasize the need to better constrain low cloud feedbacks in climate models, as they play a central role in regional cloud responses and remain a major source of uncertainty (Sherwood et al., 2020).

Our results suggest that diversity in oceanic processes contribution are influenced by the amplitude of zonal wind stress changes, suggesting that wind-driven circulation influences the warming amplitude in the equatorial band, particularly in the western Pacific. Additional analyses (Figure S6 in Supporting Information S1) comparing the relationships between $\Delta O'$ and wind stress curl changes revealed non-significant correlations, unlike the significant correlations found with zonal wind stress changes. This finding suggests that horizontal advection processes, particularly zonal advection, rather than vertical Ekman pumping, may be the dominant mechanism linking wind changes to ocean heat transport diversity across models. These wind anomalies are consistent with a weakening Walker circulation (e.g., Held & Soden, 2006; Vecchi & Soden, 2007), which may either arise from uniform warming (Ma et al., 2012; Ma & Xie, 2013), suggesting a forced oceanic response to Walker circulation changes, or from a coupled response where the warming pattern feeds back on the wind via the Bjerknes feedback (Fu & Fedorov, 2023), with inter-model variability in this feedback (Planton et al., 2021), modulating the El Niño-like warming triggered by differential evaporative cooling. Additionally, since atmospheric experiments show that the Hadley cell is more sensitive to equatorial SST gradients than the Walker cell, heat transport by

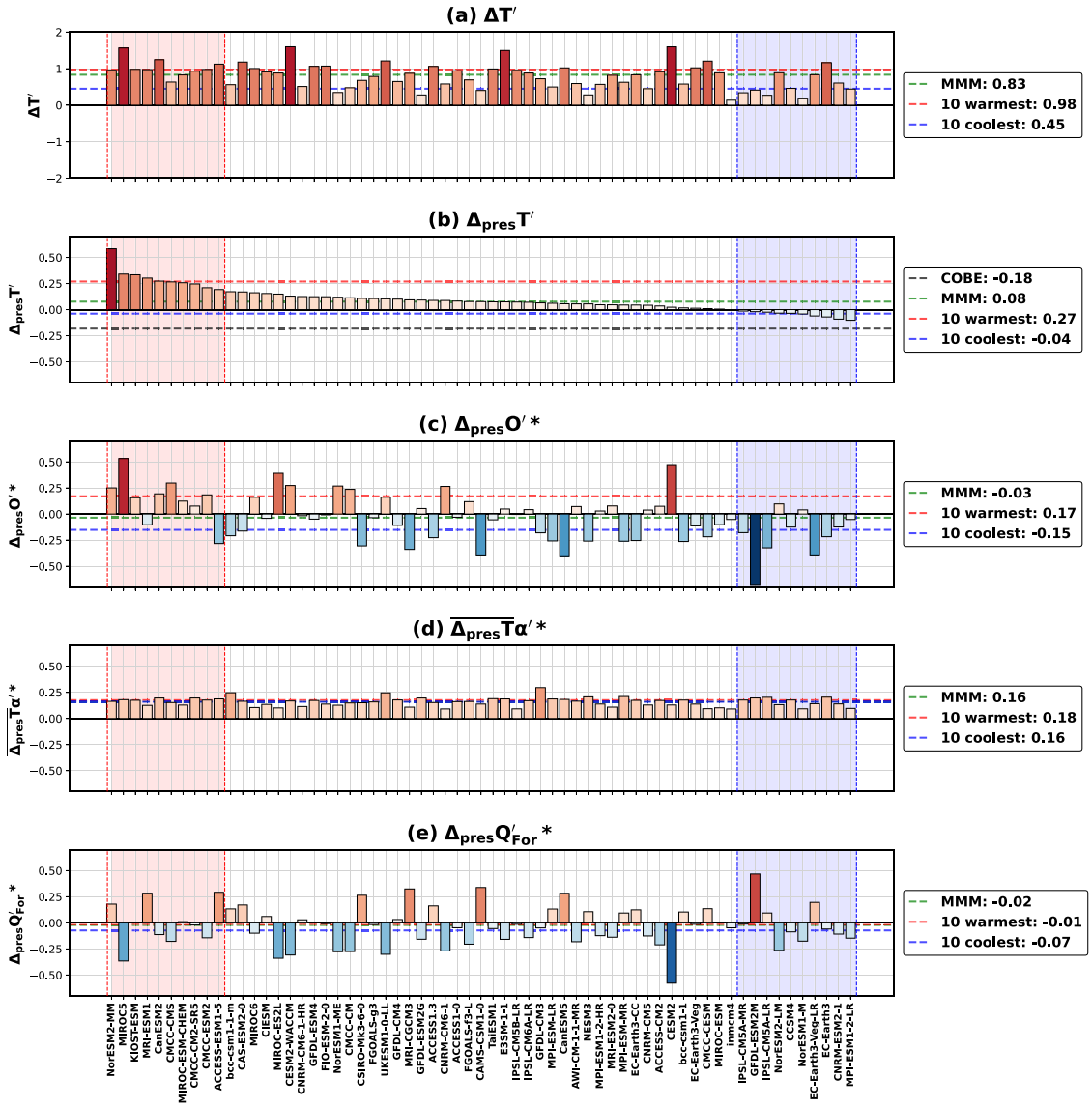

Figure 11. Drivers of present-day $\Delta_{pres}T'$ in the Eastern Equatorial Pacific (EEP). (a) Future relative SST changes ($\Delta T'$) and (b) present-day relative SST changes ($\Delta_{pres}T'$) in Coupled Model Intercomparison Project models over the EEP. Decomposition of $\Delta_{pres}T'$ into contributions from: (c) $\Delta_{pres}O'*$, (d) $\alpha'\overline{\Delta_{pres}T}*$, and (e) $\Delta_{pres}Q_{For}{}'*$. Models are ordered by their present-day $\Delta_{pres}T'$ values in all panels. The color scale represents the magnitude of each component: red indicates positive values and blue indicates negative values. The red-shaded region highlights the 10 models with the largest $\Delta_{pres}T'$ (strongest warming), while the blue-shaded region indicates the 10 models with the smallest $\Delta_{pres}T'$ (strongest cooling). Horizontal lines denote the median for the 10 warmest models (red), the 10 coolest models (blue), and the multi-model mean (MMM, green).

meridional atmospheric and oceanic circulations may offer an alternative explanation for inter-model diversity (Graffino et al., 2021; Stuecker et al., 2020).

In the eastern Pacific, oceanic processes are linked to the magnitude of the historical cold tongue bias, in addition to zonal wind stress changes. A stronger cold tongue bias indicates vigorous upwelling and an intensified ocean thermostat effect, which limits warming (Clement et al., 1996; DiNezio et al., 2009; Ying et al., 2019). While this mechanism weakens over time as warming penetrates deeper into the ocean (Heede & Fedorov, 2021), it may persist longer in scenarios with gradual greenhouse gas increases compared to abrupt CO2 doubling experiments, as used by these authors.

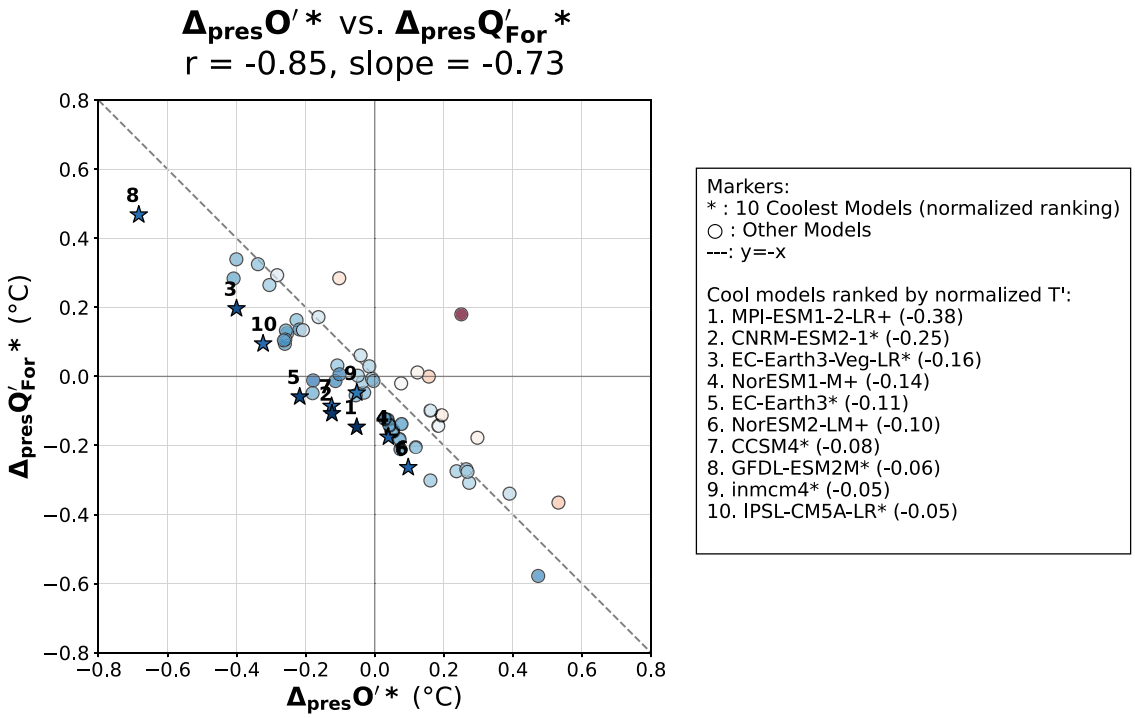

Figure 12. Relationship between processes driving $\Delta_{pres}T'$ in the Eastern Equatorial Pacific. Scatterplot of $\Delta_{pres}Q_{For}{}'*$ versus $\Delta_{pres}O'*$ across models. Colors reflects $\Delta_{pres}T'$ magnitude, where red indicates warming and blue indicates cooling. Stars denote the 10 models with the cooler $\Delta_{pres}T'$, ranked by their cooling magnitude (numbers indicate rank). The dashed line represents the relationship $y = -x$.

Our analysis over the present-day period finally reveals similar drivers of the MMM and inter-model diversity as in future projections. However, only a subset of models reproduce a relative cooling trend in the eastern Pacific as in observations, albeit weaker. Among the 10 models most aligned with observations, cooling arises from diverse mechanisms: oceanic processes dominate in three, air-sea fluxes in two, and a combination of both in five. This diversity underscores the need for process-based studies across multiple models to fully understand the discrepancies between observed and modeled warming patterns.

Conflict of Interest

The authors declare no conflicts of interest relevant to this study.

Data Availability Statement

All the CMIP data (Eyring et al., 2016; Taylor et al., 2012) are available from the Earth System Grid Federation (ESGF) server (https://esgf-node.llnl.gov/projects/esgf-llnl/). COBE SST data sets are available from the NOAA/OAR/ESRL PSD website (https://www.esrl.noaa.gov/psd/data/gridded/).

The software and analysis scripts used to generate the results and figures can be accessed using the following DOI link https://doi.org/10.5281/zenodo.15202963 (Danielli, 2025).

Acknowledgments
We would like to thank the World Climate Research Program's Working Group on Coupled Modeling, which produced and made available the CMIP models outputs. This research was funded by the Pacific Community. The funders had no role in the design of the study; in the collection, analyses, or interpretation of data; in the writing of the manuscript, nor in the decision to publish the results.

References

Bjerknes, J. (1969). Monthly weather reyiew atmospheric teleconnections from the equatorial Pacific. *Monthly Weather Review*, *97*(3), 163–172. https://doi.org/10.1175/1520-0493(1969)097<0163:atftep>2.3.co;2

Cai, W., Borlace, S., Lengaigne, M., Van Rensch, P., Collins, M., Vecchi, G., et al. (2014). Increasing frequency of extreme El Niño events due to greenhouse warming. *Nature Climate Change*, *4*(2), 111–116. https://doi.org/10.1038/nclimate2100

Cai, W., Wu, L., Lengaigne, M., Li, T., McGregor, S., Kug, J. S., et al. (2019). Pantropical climate interactions. *Science*, *363*(6430), eaav4236. https://doi.org/10.1126/science.aav4236

Clement, A. C., Seager, R., Cane, M. A., & Zebiak, S. E. (1996). An Ocean dynamical thermostat. *Journal of Climate*, *9*(9), 2190–2196. https://doi.org/10.1175/1520-0442(1996)009<2190:AODT>2.0.CO;2

Danielli, V. (2025). *Earth's future "Drivers of CMIP tropical Pacific warming pattern diversity" software* (version v2) [Software]. *Zenodo*. https://doi.org/10.5281/zenodo.15202963

DiNezio, P. N., Clement, A. C., Vecchi, G. A., Soden, B. J., Kirtman, B. P., & Lee, S. K. (2009). Climate response of the equatorial Pacific to global warming. *Journal of Climate*, *22*(18), 4873–4892. https://doi.org/10.1175/2009JCLI2982.1

Dong, Y., Armour, K. C., Battisti, D. S., & Blanchard-Wrigglesworth, E. (2022). Two-way teleconnections between the Southern Ocean and the tropical Pacific via a dynamic feedback. *Journal of Climate*, *35*(19), 2667–2682. https://doi.org/10.1175/JCLI-D-22-0080.1

Eyring, V., Bony, S., Meehl, G. A., Senior, C. A., Stevens, B., Stouffer, R. J., & Taylor, K. E. (2016). Overview of the coupled model Intercomparison project phase 6 (CMIP6) experimental design and organization. *Geoscientific Model Development*, *9*(5), 1937–1958. https://doi.org/10.5194/gmd-9-1937-2016

Fu, M., & Fedorov, A. (2023). The role of Bjerknes and shortwave feedbacks in the tropical Pacific SST response to global warming. *Geophysical Research Letters*, *50*(19), e2023GL105061. https://doi.org/10.1029/2023GL105061

Gopika, S., Lengaigne, M., Suresh, I., Izumo, T., Kwatra, S., Neetu, S., & Vialard, J. (2024). Assessing CMIP models' ability to detect observed surface warming signals related to climate change. https://doi.org/10.1175/JCLI-D-24

Graffino, G., Farneti, R., & Kucharski, F. (2021). Low-frequency variability of the Pacific Subtropical Cells as reproduced by coupled models and ocean reanalyses. *Climate Dynamics*, *56*(9–10), 3231–3254. https://doi.org/10.1007/s00382-021-05639-6

Grise, K. M., Davis, S. M., Simpson, I. R., Waugh, D. W., Fu, Q., Allen, R. J., et al. (2019). Recent tropical expansion: Natural variability or forced response? *Journal of Climate*, *28*(8), 1551–1571. https://doi.org/10.1175/JCLI

Grise, K. M., & Polvani, L. M. (2016). Is climate sensitivity related to dynamical sensitivity? *Journal of Geophysical Research*, *121*(10), 5159–5176. https://doi.org/10.1002/2015JD024687

Guan, C., & McPhaden, M. J. (2016). Ocean processes affecting the twenty-first-century shift in ENSO SST variability. *Journal of Climate*, *29*(19), 6861–6879. https://doi.org/10.1175/JCLI-D-15-0870.1

Guan, C., McPhaden, M. J., Wang, F., & Hu, S. (2019). Quantifying the role of oceanic feedbacks on ENSO Asymmetry. *Geophysical Research Letters*, *46*(4), 2140–2148. https://doi.org/10.1029/2018GL081332

Heede, U. K., & Fedorov, A. V. (2021). Eastern equatorial Pacific warming delayed by aerosols and thermostat response to CO2 increase. *Nature Climate Change*, *11*(8), 696–703. https://doi.org/10.1038/s41558-021-01101-x

Heede, U. K., & Fedorov, A. V. (2023). Colder eastern equatorial Pacific and stronger walker circulation in the early 21st century: Separating the forced response to global warming from natural variability. *Geophysical Research Letters*, *50*(3), e2022GL101020. https://doi.org/10.1029/2022GL101020

Heede, U. K., Fedorov, A. V., & Burls, N. J. (2020). Time scales and mechanisms for the tropical Pacific response to global warming: A tug of war between the ocean thermostat and weaker walker. *Journal of Climate*, *33*(14), 6101–6118. https://doi.org/10.1175/JCLI-D-19-0690.1

Heede, U. K., Fedorov, A. V., & Burls, N. J. (2021). A stronger versus weaker walker: Understanding model differences in fast and slow tropical Pacific responses to global warming. *Climate Dynamics*, *57*(9–10), 2505–2522. https://doi.org/10.1007/s00382-021-05818-5

Held, I. M., & Soden, B. J. (2006). Robust responses of the hydrological cycle to global warming. *Journal of Climate*, *19*(21), 5686–5699. https://doi.org/10.1175/jcli3990.1

Hirahara, S., Ishii, M., & Fukuda, Y. (2014). Centennial-scale sea surface temperature analysis and its uncertainty. *Journal of Climate*, *27*(1), 57–75. https://doi.org/10.1175/JCLI-D-12-00837.1

Huang, P., & Ying, J. (2015). A multimodel ensemble pattern regression method to correct the tropical Pacific SST change patterns under global warming. *Journal of Climate*, *28*(12), 4706–4723. https://doi.org/10.1175/JCLI-D-14-00833.1

Hwang, Y. T., Xie, S. P., Chen, P. J., Tseng, H. Y., & Deser, C. (2024). Contribution of anthropogenic aerosols to persistent La Niña-like conditions in the early 21st century. *Proceedings of the National Academy of Sciences of the United States of America*, *121*(5), e2315124121. https://doi.org/10.1073/pnas.2315124121

Izumo, T., Vialard, J., Lengaigne, M., & Suresh, I. (2020). Relevance of relative sea surface temperature for tropical rainfall interannual variability. *Geophysical Research Letters*, *47*(3), e2019GL086182. https://doi.org/10.1029/2019GL086182

Jebri, B., Khodri, M., Echevin, V., Gastineau, G., Thiria, S., Vialard, J., & Lebas, N. (2020). Contributions of internal variability and external forcing to the recent trends in the southeastern Pacific and Peru-chile upwelling system. *Journal of Climate*, *33*(24), 10555–10578. https://doi.org/10.1175/JCLI-D-19-0304.1

Johnson, N. C., & Xie, S. P. (2010). Changes in the sea surface temperature threshold for tropical convection. *Nature Geoscience*, *3*(12), 842–845. https://doi.org/10.1038/ngeo1008

Kang, S. M., Shin, Y., Kim, H., Xie, S. P., & Hu, S. (2023). Disentangling the mechanisms of equatorial Pacific climate change. *Science Advances*, *9*(19), 1–9. https://doi.org/10.1126/sciadv.adf5059

Kang, S. M., Xie, S.-P., Shin, Y., Kim, H., Hwang, Y.-T., Stuecker, M. F., et al. (2020). Walker circulation response to extratropical radiative forcing. *Science Advances*, *6*(47), eabd3021. https://doi.org/10.1126/sciadv.abd3021

Kent, C., Chadwick, R., & Rowell, D. P. (2015). Understanding uncertainties in future projections of seasonal tropical precipitation. *Journal of Climate*, *28*(11), 4390–4413. https://doi.org/10.1175/JCLI-D-14-00613.1

Kim, H., Kang, S. M., Kay, J. E., Xie, S.-P., & Hartmann, D. (2022). Subtropical clouds key to Southern Ocean teleconnections to the tropical Pacific. https://doi.org/10.1073/pnas

Lee, S., L'Heureux, M., Wittenberg, A. T., Seager, R., O'Gorman, P. A., & Johnson, N. C. (2022). On the future zonal contrasts of equatorial Pacific climate: Perspectives from Observations, Simulations, and Theories. *Npj Climate and Atmospheric Science*, *5*(1), 82. https://doi.org/10.1038/s41612-022-00301-2

Li, G., Xie, S. P., Du, Y., & Luo, Y. (2016). Effects of excessive equatorial cold tongue bias on the projections of tropical Pacific climate change. Part I: The warming pattern in CMIP5 multi-model ensemble. *Climate Dynamics*, *47*(12), 3817–3831. https://doi.org/10.1007/s00382-016-3043-5

Lin, J. L., Qian, T., & Shinoda, T. (2014). Stratocumulus clouds in Southeastern Pacific simulated by eight CMIP5-CFMIP global climate models. *Journal of Climate*, *27*(8), 3000–3022. https://doi.org/10.1175/JCLI-D-13-00376.1

Liu, Z., & Alexander, M. (2007). Atmospheric bridge, oceanic tunnel, and global climatic teleconnections. *Reviews of Geophysics*, *45*(2). https://doi.org/10.1029/2005RG000172

Liu, Z., Vavrus, S., He, F., Wen, N., & Zhong, Y. (2005). Rethinking tropical ocean response to global warming: The enhanced equatorial warming. *Journal of Climate*, *18*(22), 4684–4700. https://doi.org/10.1175/JCLI3579.1

Ma, J., & Xie, S. P. (2013). Regional patterns of sea surface temperature change: A source of uncertainty in future projections of precipitation and atmospheric circulation. *Journal of Climate*, *26*(8), 2482–2501. https://doi.org/10.1175/JCLI-D-12-00283.1

Ma, J., Xie, S. P., & Kosaka, Y. (2012). Mechanisms for tropical tropospheric circulation change in response to global warming. *Journal of Climate*, *25*(8), 2979–2994. https://doi.org/10.1175/JCLI-D-11-00048.1

Park, C., Kang, S. M., Stuecker, M. F., & Jin, F. F. (2022). Distinct surface warming response over the Western and eastern equatorial Pacific to radiative forcing. *Geophysical Research Letters*, *49*(2), 1–10. https://doi.org/10.1029/2021GL095829

Planton, Y. Y., Guilyardi, E., Wittenberg, A. T., Lee, J., Gleckler, P. J., Bayr, T., et al. (2021). Evaluating climate models with the CLIVAR 2020 ENSO metrics package. In *Bulletin of the American Meteorological Society* (Vol. 102, Iss. (2), pp. E193–E217). https://doi.org/10.1175/BAMS-D-19-0337.1

Power, S., Lengaigne, M., Capotondi, A., Khodri, M., Vialard, J., Jebri, B., et al. (2021). Decadal climate variability in the tropical Pacific: Characteristics, causes, predictability, and prospects. *Science*, *374*(6563), eaay9165. https://doi.org/10.1126/science.aay9165

Ramanathan, V., & Collins, W. (1991). Thermodynamic regulation of ocean warming by cirrus clouds deduced from observations of the 1987 El Niño. *Nature*, *351*(6321), 27–32. https://doi.org/10.1038/351027a0

Seager, R., Cane, M., Henderson, N., Lee, D. E., Abernathey, R., & Zhang, H. (2019). Strengthening tropical Pacific zonal sea surface temperature gradient consistent with rising greenhouse gases. *Nature Climate Change*, *9*(7), 517–522. https://doi.org/10.1038/s41558-019-0505-x

Seager, R., Henderson, N., & Cane, M. (2022). Persistent discrepancies between observed and modeled trends in the tropical Pacific ocean. *Journal of Climate*, *35*(14), 4571–4584. https://doi.org/10.1175/JCLI-D-21-0648.1

Sherwood, S. C., Webb, M. J., Annan, J. D., Armour, K. C., Forster, P. M., Hargreaves, J. C., et al. (2020). An assessment of Earth's climate sensitivity using multiple lines of evidence. In *Reviews of Geophysics* (Vol. 58, Iss. (4)). e2019RG000678, Blackwell Publishing Ltd. https://doi.org/10.1029/2019RG000678

Sobel, A. H., Lee, C.-Y., Bowen, S. G., Camargo, S. J., Cane, M. A., Clement, A., et al. (2023). Near-term tropical cyclone risk and coupled Earth system model biases. *Proceedings of the National Academy of Sciences of the United States of America*, *120*(33), e2209631120. https://doi.org/10.1073/pnas.2209631120/-/DCSupplemental

Stevens, B., Sherwood, S. C., Bony, S., & Webb, M. J. (2016). Prospects for narrowing bounds on Earth's equilibrium climate sensitivity. *Earth's Future*, *4*(11), 512–522. https://doi.org/10.1002/2016EF000376

Stuecker, M. F., Timmermann, A., Jin, F. F., Proistosescu, C., Kang, S. M., Kim, D., et al. (2020). Strong remote control of future equatorial warming by off-equatorial forcing. *Nature Climate Change*, *10*(2), 124–129. https://doi.org/10.1038/s41558-019-0667-6

Takahashi, N., Richards, K. J., Schneider, N., Stuecker, M. F., Annamalai, H., & Nonaka, M. (2023). Observed relative contributions of anomalous heat fluxes and effective heat capacity to sea surface temperature variability. *Geophysical Research Letters*, *50*(17). https://doi.org/10.1029/2023GL103165

Taylor, K. E., Stouffer, R. J., & Meehl, G. A. (2012). An overview of CMIP5 and the experiment design. In *Bulletin of the American Meteorological Society* (Vol. 93, Issue (4), pp. 485–498). https://doi.org/10.1175/BAMS-D-11-00094.1

Tseng, H. Y., Hwang, Y. T., Xie, S. P., Tseng, Y. H., Kang, S. M., Luongo, M. T., & Eisenman, I. (2023). Fast and slow responses of the tropical Pacific to radiative forcing in northern high latitudes. *Journal of Climate*, *36*(16), 5337–5349. https://doi.org/10.1175/JCLI-D-22-0622.1

Vecchi, G. A., Clement, A., & Soden, B. J. (2008). Examining the tropical Pacific's response to global warming. *Eos*, *89*(9), 81–83. https://doi.org/10.1029/2008EO090002

Vecchi, G. A., & Soden, B. J. (2007). Global warming and the weakening of the tropical circulation. *Journal of Climate*, *20*(17), 4316–4340. https://doi.org/10.1175/JCLI4258.1

Watanabe, M., Dufresne, J. L., Kosaka, Y., Mauritsen, T., & Tatebe, H. (2021). Enhanced warming constrained by past trends in equatorial Pacific sea surface temperature gradient. *Nature Climate Change*, *11*(1), 33–37. https://doi.org/10.1038/s41558-020-00933-3

Watanabe, M., Kang, S. M., Collins, M., Hwang, Y. T., McGregor, S., & Stuecker, M. F. (2024). Possible shift in controls of the tropical Pacific surface warming pattern. *Nature*, *630*(8016), 315–324. https://doi.org/10.1038/s41586-024-07452-7

Wills, R. C. J., Dong, Y., Proistosecu, C., Armour, K. C., & Battisti, D. S. (2022). Systematic climate model biases in the large-scale patterns of recent sea-surface temperature and sea-level pressure change. *Geophysical Research Letters*, *49*(17), e2022GL100011. https://doi.org/10.1029/2022GL100011

Xie, S. (2020). Ocean warming pattern effect on global and regional climate change. *AGU Advances*, *1*(1), e2019AV000130. https://doi.org/10.1029/2019av000130

Xie, S. P., Deser, C., Vecchi, G. A., Ma, J., Teng, H., & Wittenberg, A. T. (2010). Global warming pattern formation: Sea surface temperature and rainfall. *Journal of Climate*, *23*(4), 966–986. https://doi.org/10.1175/2009JCLI3329.1

Ying, J., & Huang, P. (2016). Cloud-radiation feedback as a leading source of uncertainty in the tropical Pacific SST warming pattern in CMIP5 models. *Journal of Climate*, *29*(10), 3867–3881. https://doi.org/10.1175/JCLI-D-15-0796.1

Ying, J., Huang, P., & Huang, R. (2015). Evaluating the formation mechanisms of the equatorial Pacific SST warming pattern in CMIP5 models. *Advances in Atmospheric Sciences*, *33*(4), 433–441. https://doi.org/10.1007/s00376-015-5184-6

Ying, J., Huang, P., Lian, T., & Tan, H. (2019). Understanding the effect of an excessive cold tongue bias on projecting the tropical Pacific SST warming pattern in CMIP5 models. *Climate Dynamics*, *52*(3–4), 1805–1818. https://doi.org/10.1007/s00382-018-4219-y

Zhang, L., & Li, T. (2014). A simple analytical model for understanding the formation of sea surface temperature patterns under global warming. *Journal of Climate*, *27*(22), 8413–8421. https://doi.org/10.1175/JCLI-D-14-00346.1

Zhou, Z. Q., & Xie, S. P. (2015). Effects of climatological model biases on the projection of tropical climate change. *Journal of Climate*, *28*(24), 9909–9917. https://doi.org/10.1175/JCLI-D-15-0243.1